A PERTURBATION EXPANSION APPROACH TO SOLVING THE ELECTROMAGNETIC INDUCTION PROBLEM IN THREE DIMENSIONS

By

Nancy H. Natek

Submitted in Partial Fulfillment
of the Requirements for the

Master of Science in Geophysics

New Mexico Institute of Mining and Technology
Department of Earth and Environmental Science

Socorro, New Mexico

December 2004

ABSTRACT

The objective of this modeling study is to investigate the 3D electromagnetic induction problem for a single transmitter/receiver sonde approaching a fault within a hydrocarbon reservoir. The fault-bounded reservoir is modeled as an anomalous quarterspace embedded within a relatively conductive one siemens/meter homogeneous formation. Its electromagnetic response is computed in the frequency domain using a truncated perturbation expansion about the response of the reservoir-free formation. The first term of the expansion is derived considering an adjoint equation approach. Higher-order terms can be found similarly but are not considered here.

ACKNOWLEDGEMENTS

I would especially like to thank Dr. Chester J. Weiss at the Geophysical Technology Department, Sandia National Laboratories, for the opportunity to work on this project and participate in the Student Internship Program and for the use of his magnetic dipole anisotropic code. I would also like to thank Dr. Harold J. Tobin at the Earth and Environmental Sciences Department, New Mexico Tech, for supervision and discussions, Dr. Richard C. Aster at the Earth and Environmental Sciences Department, New Mexico Tech for academic discussions. I would like to express my appreciation to Tilman Hanstein of KMS Technologies for the use of his inverse digital filters Fourier transform code, and to the High Performance Computing Center at the University of New Mexico for the use of its computational resources and for technical support. I would also like to thank the Natural Gas and Oil Technology Partnership (NGOTP) for supporting this work. Most importantly, I would like to thank my husband Paul for his constant love and continuing support.

TABLE OF CONTENTS

	Page
INTRODUCTION	1
SENSITIVITY COMPUTATION	3
ALGORITHM SUMMARY	11
SENSITVITY RESULTS	15
INTERPRETATION OF SENSITIVITIES	19
Plotting the Integrand	25
Sensitivities in Oblique Planes	26
CONCLUSIONS	29
BIBLIOGRAPHY	33
APPENDIX A – The Anisotropic Case	73
APPENDIX B – The Numerical Code	79

LIST OF FIGURES

Figure	Page
Figure 1. The induction sonde	35
Figure 2. The quarterspace fault model	36
Figure 3. Spatial dependence of the magnitude of the electric field	37
Figure 4. Sensitivities in the frequency domain above and below the FBC	38
Figure 5. Sensitivities in the time domain above and below the FBC	39
Figure 6. Sensitivities in the frequency domain around the FBC	40
Figure 7. Sensitivities in the time domain around the FBC	41
Figure 8. Sensitivities in the frequency and time domain relative to the FBC	42
Figure 9. Symmetry of response in the frequency domain	43
Figure 10. Symmetry of response in the time domain	44
Figure 11: Tool locations around the fault boundary corner	45
Figure 12. Frequency domain for tool 1, frequency = 20,000 Hz	46
Figure 13. Frequency domain for tool 2, receiver dipole in the *y*-direction	47
Figure 14. Frequency domain for tool 2, receiver dipole in the *z*-direction	48
Figure 15. Frequency domain for tool 1, frequency = 2000 Hz	49
Figure 16. Frequency domain for tool 1, frequency = 200 Hz	50
Figure 17. The integration over *x*	51
Figure 18. The integrand for tool 2, receiver dipole in the *x*-direction	52

Figure 19. The keyhole feature 53

Figure 20. Strongest vs. weakest magnitudes of the sensitivities 54

Figure 21. Overall magnitude of the sensitivities 55

Figure 22. Real and imaginary sensitivity values for various conductivities 56

Figure 23. Real and imaginary sensitivity values five meters from the FBC 57

Figure 24. Real and imaginary sensitivity values ten meters from the FBC 58

Figure 25. Real and imaginary sensitivity values for various tool locations 59

Figure 26. Plotting the integrand in the frequency domain 60

Figure 27. The integrand for $\theta = 0°$, receiver dipole in the sonde direction 61

Figure 28. The integrand for $\theta = 45°$, receiver dipole in the sonde direction 62

Figure 29. The integrand for $\theta = 90°$, receiver dipole in the sonde direction 63

Figure 30. The integrand for tool 1, around the FBC 64

Figure 31. The integrand for tool 1, five and ten meters from the FBC 65

Figure 32. Map projection of the fault boundary corner 66

Figure 33: Tool locations around the fault boundary corner 67

Figure 34. Sensitivities in the oblique plane, for receiver dipole along sonde 68

Figure 35. Sensitivities in the oblique plane, for receiver dipole along sonde 69

Figure 36. Sensitivities in the oblique plane, receiver dipole in the *x*-direction 70

Figure 37. Sensitivities in the oblique planes around the FBC 71

Figure 38. The oblique planes, receiver dipoles in the *x ,y, z*-directions 72

LIST OF TABLES

Page

Table 1. Hertz vector for a magnetic dipole in a homogeneous anisotropic case 77

INTRODUCTION

The primary objective of geophysical well logging for petroleum is to identify potential reservoir rocks by determining their porosity and permeability, and the nature and volume of fluids present. Water saturation and porosity measurements can provide distinguishing traits of hydrocarbon-bearing formations. Archie (1942) developed empirical equations, used in petroleum work today, to relate resistivity measurements of a formation to its porosity and water saturation. Known as Archie's law, it is expressed as

$$FF = a\phi^{-m}, \tag{1}$$

where FF is known as the formation factor (the ratio of the formation resistivity to the pore fluids), ϕ is the porosity, m is the cementation factor and a is a constant that varies with rock type. Formations saturated with oil have a higher resistivity versus formations saturated with saline water; therefore high resistivity readings can denote hydrocarbon-bearing formations.

An induction sonde (Figure 1) is a tool designed to measure formation resistivity in boreholes. A multi-component induction sonde consists of a transmitter and receiver coil, typically with offsets of one to three meters. For higher resolutions, multiple transmitter and receiver coils may be used. As the induction sonde is lowered into the borehole, a time-varying magnetic field produced by the transmitter coil induces eddy currents in conductive formation. These eddy currents in turn induce secondary magnetic fields measured in the receiver coil in an electromagnetic field. These secondary fields are direct indicators of the formation conductivity (Telford *et al*., 1990).

Doll (1949) developed the first commercial induction tool in the late 1940's for the Schlumberger Well Surveying Corporation. Doll derived an approximate model for tool

response based on his “geometrical factor” concept in which non-interacting eddy currents are induced in the formation. The eddy currents are considered to be concentric with the simplest configuration in which the transmitter and receiver close are together (one meter offset), with the transmitter and receiver dipoles in the direction of the tool orientation (Moran and Kunz, 1962, Dyck, 1988).

There has been extensive work in developing computer codes to model induction tool logs. Codes have been developed to model the layered earth (Anderson and Gianzero, 1983), a layered earth at dip (Anderson, *et al*., 1986) and with anisotropic conductivity (Moran and Gianzero, 1979; Anderson, *et al*., 1995). Recent advances in modeling at Sandia National Laboratories include modeling low frequency electromagnetic induction in a fully 3D anisotropic earth (Weiss and Newman, 2002; 2003). A more extensive history of induction well logging and computer modeling in log interpretation can be found in Anderson (2001).

The objective of our modeling study is to investigate the 3D electromagnetic induction problem for a single transmitter/receiver sonde approaching a fault within a hydrocarbon reservoir. The fault-bounded reservoir is modeled as an anomalous quarterspace embedded within a relatively conductive one siemens/meter homogeneous formation. Its electromagnetic response is computed in the frequency domain using a truncated perturbation expansion about the response of the reservoir-free formation. The first term of the expansion is derived considering an adjoint equation approach.

For a uniformly conducting wholespace, an analytic solution is available to calculate the electric and magnetic fields around the receiver from dipole sources at the transmitter (Ward and Hohmann, 1988). A quantity of physical interest we will look at is the

sensitivity, $\partial H/\partial\sigma$ or how the magnetic field changes at the receiver in response to perturbations from the wholespace conductivity. For an inhomogeneous case as in our quarterspace fault model (Figure 2a), electric and magnetic fields around the receiver cannot be calculated analytically due to the geometry of the problem. However, the magnetic sensitivities at the receiver can be obtained by an exact solution to the associated adjoint problem (McGillivray *et al*., 1994). Thus, a first order approximation is given by the series expansion $H \sim H_o + \Delta\sigma\ \partial H/\partial\sigma$ -- an expression that is easy and fast to calculate because it is based on simple analytic formulae.

In the most general case, the adjoint approach used here also applies to the case where σ is a tensor, and thus represents an anisotropic conductivity. We began this research with an anisotropic code (Weiss, 2002) and features of the anisotropic case will be discussed in Appendix A. However, for simplicity at analysis and minimization of computer routines, only the isotropic case is considered here.

SENSITIVITY COMPUTATION

For a uniformly conducting wholespace, an analytic solution exits for the electric and magnetic fields at the receiver arising from a point magnetic dipole source at the transmitter (Ward and Hohmann, 1988). Multiple sources are handled through superposition, however, for an inhomogeneous case as in our quarterspace fault model (Figure 1a), the electric and magnetic fields around the receiver cannot be calculated analytically due to the geometry of the problem.

A quantity of physical interest is the *sensitivity*, $\partial\vec{H}/\partial\sigma$, or the variation of the fields at the receiver due to a conductivity perturbation in the media. McGillivray *et al*. (1994)

present a derivation to compute the sensitivities (or Frechet derivatives) needed to solve the inverse problems in electromagnetic induction. The magnetic sensitivities can be obtained by an approximation (the adjoint method) by solving two boundary-value problems. The primary problem is first solved beginning with Maxwell's equations:

$$\begin{aligned} \nabla \times \vec{E} &= -i\omega\mu\left(\vec{H} + \vec{M}\right)_s, \\ \nabla \times \vec{H} &= \left(\sigma + i\omega\varepsilon\right)\vec{E} + \vec{J}_s, \end{aligned} \tag{2}$$

where $\vec{E}$ and $\vec{H}$ are the electric and magnetic field strengths, $\vec{M}_s$ and $\vec{J}_s$ are the magnetic and electric current densities respectively, μ is the magnetic susceptibility, ε is the electrical permittivity, σ is the conductivity and

$$\begin{aligned} \vec{B} &= \mu\vec{H} + \mu\vec{M}_s, \\ \vec{J} &= \vec{\sigma}\vec{E} + \vec{J}_s, \\ \vec{D} &= \varepsilon\vec{E}. \end{aligned}$$

The above are Maxwell's equations in the frequency domain where all fields are assumed to have the time dependence $e^{i\omega t}$, with angular frequency ω.

The conductivity $\sigma(\vec{x})$ can be expanded in terms of a set of basis functions $\psi_j(\vec{x})$

$$\sigma(\vec{x}) = \sum_{j=1}^{M} \sigma_j \psi_j(\vec{x}), \tag{3}$$

where σ_j are real constants. $\sigma(\vec{x})$ is then specified by an M-vector $\vec{\sigma} = (\sigma_1.\sigma_2,...,\sigma_M)$. For example, in a layered model it would be convenient to choose the basis as

$$\psi_j(\vec{x}) = \begin{cases} 1 & x \in \text{layer j} \\ 0 & x \notin \text{layer j} \end{cases}.$$

Thus σ_j represents the layer conductivities. Clearly other choices of $\psi_j(\vec{x})$ are available (e.g. sines and cosines, spherical harmonics, Tchebyshevs, etc.) and the selection of the

right basis is dependent upon the problem at hand. For now, we retain the general form, Eq.(3) and proceed with the derivation of $\partial\vec{H}/\partial\sigma$.

In the inverse problem, McGillivray *et al*. compute the sensitivities $G_{ik} = \left(\partial d_i/\partial\sigma_k\right)$, where d_i is the *i*th datum, by computing $\partial\vec{E}/\partial\sigma_k$ and $\partial\vec{H}/\partial\sigma_k$. Substituting Eq.(3) into Eq.(2) and differentiating with respect to σ_k produces the sensitivity equation for the electric field:

$$\nabla\times\frac{\partial\vec{E}}{\partial\sigma_k} = -i\omega\mu\left(\frac{\partial\vec{H}}{\partial\sigma_k} + \frac{\partial\vec{M}_s}{\partial\sigma_k}\right).$$

Since $\vec{M}_s$ does not depend on σ, i.e. $\vec{M}_s = \vec{M}_s\left(\vec{x}\right) \neq \vec{M}_s\left(\vec{x},\sigma\right)$, then

$$\nabla\times\frac{\partial\vec{E}}{\partial\sigma_k} = -i\omega\mu\frac{\partial\vec{H}}{\partial\sigma_k}. \tag{4a}$$

Likewise, the sensitivity equation for the magnetic field is determined by differentiating the second equation in Eq.(2) to obtain

$$\nabla\times\frac{\partial\vec{H}}{\partial\sigma_k} = \left[\frac{\partial}{\partial\sigma_k}\left(\sigma + i\omega\varepsilon\right)\right]\vec{E} + \left(\sigma + i\omega\varepsilon\right)\frac{\partial\vec{E}}{\partial\sigma_k} + \frac{\partial\vec{J}_s}{\partial\sigma_k}.$$

Since $\vec{J}_s$ does not depend on σ, i.e. $\vec{J}_s = \vec{J}_s\left(\vec{x}\right) \neq \vec{J}_s\left(\vec{x},\sigma\right)$, then

$$\nabla\times\frac{\partial\vec{H}}{\partial\sigma_k} = \left[\frac{\partial\sigma}{\partial\sigma_k}\right]E + \left(\sigma + i\omega\varepsilon\right)\frac{\partial\vec{E}}{\partial\sigma_k}.$$

From $\sigma = \sum_{k=1}^{m}\sigma_k\psi_k = \sigma_1\psi_1 + \sigma_2\psi_2 + ... + \sigma_m\psi_m$, we have

$$\frac{\partial\sigma}{\partial\sigma_k} = \psi_k,$$

which yields

$$\nabla\times\frac{\partial\vec{H}}{\partial\sigma_k} = \psi_k\vec{E} + \left(\sigma + i\omega\varepsilon\right)\frac{\partial\vec{E}}{\partial\sigma_k}. \tag{4b}$$

Our goal is to derive equations from which we can compute $\partial\vec{H}/\partial\sigma_k$, $\partial\vec{E}/\partial\sigma_k$ using only equations of the form in Eq.(2). We then consider an auxiliary problem similar to Eq.(2) in which all the fields are replaced by $\vec{E} \to \tilde{\vec{E}}$, etc…

$$\begin{aligned} \nabla \times \tilde{\vec{E}} &= -i\omega\mu\left(\tilde{\vec{H}} + \tilde{\vec{M}}\right)_s \\ \nabla \times \tilde{\vec{H}} &= \left(\sigma + i\omega\varepsilon\right)\tilde{\vec{E}} + \tilde{\vec{J}}_s \end{aligned} \tag{5}$$

where the electric and magnetic sources $\tilde{\vec{J}}_s$, $\tilde{\vec{M}}_s$ have not yet been defined. With the use of the vector identity,

$$\vec{\nabla} \cdot \left(\vec{A} \times \vec{B}\right) = \vec{B} \cdot \left(\vec{\nabla} \times \vec{A}\right) - \vec{A} \cdot \left(\vec{\nabla} \times \vec{B}\right), \tag{6}$$

Eq.(4a), Eq.(4b) and Eq.(5) can be combined to form

$$\begin{aligned} &\vec{\nabla} \cdot \left(\tilde{\vec{E}} \times \frac{\partial\vec{H}}{\partial\sigma_k} - \frac{\partial\vec{E}}{\partial\sigma_k} \times \tilde{\vec{H}}\right) \\ &\quad = \tilde{\vec{M}}_s \cdot \frac{\partial\vec{H}}{\partial\sigma_k} + \tilde{J}_s \frac{\partial\vec{E}}{\partial\sigma_k} - \tilde{\vec{E}} \cdot \vec{E}\psi_k(\vec{x}). \end{aligned} \tag{7}$$

Note that $i\omega\mu$ and $\sigma + i\omega t$ cancel identically. Integrating over the domain D and using the divergence theorem gives

$$\begin{aligned} &\int_{\partial D} \left(\tilde{\vec{E}} \times \frac{\partial\vec{H}}{\partial\sigma_k} - \frac{\partial\vec{E}}{\partial\sigma_k} \times \tilde{\vec{H}}\right) \cdot \vec{n} ds \\ &\quad = \int_{\partial D} \left[\tilde{\vec{M}}_s \cdot \frac{\partial\vec{H}}{\partial\sigma_k} + \tilde{J}_s \cdot \frac{\partial\vec{E}}{\partial\sigma_k} - \tilde{\vec{E}} \cdot \vec{E}\psi_k(\vec{x})\right] \, d\text{v}. \end{aligned} \tag{8}$$

The desired result is obtained when the left hand side can be shown to be equal to zero, which depends on the extent of the boundary. As the boundary ∂D extends to infinity, the LHS can be shown to approach zero, while for the case of a finite domain the LHS is again zero if the primary and auxiliary problems have the same boundary conditions (McGillivray *et al*, 1994). In both cases, setting the LHS of Eq.(8) to zero yields

$$\int_D \left(\tilde{\vec{M}}_s \cdot \frac{\partial \vec{H}}{\partial \sigma_k} + \tilde{J}_s \frac{\partial \vec{E}}{\partial \sigma_k} \right) \, d\mathrm{v} = \int_D \tilde{\vec{E}} \cdot \vec{E} \;\; \psi_k(\vec{x}) \;\; d\mathrm{v}. \tag{9}$$

This is the central equation from which the sensitivities can be computed.

Consider the following example that forms the basis for the research presented in this work; a point magnetic dipole of strength m located at $\vec{x}_0$, pointing in the x-direction, and no electric current density $\tilde{\vec{J}}_s = 0$. This gives rise to a magnetization vector $\tilde{\vec{M}}_s = \delta(\vec{x} - \vec{x}_0)\hat{x}$. Substituting these expressions into Eq.(9) yields an equation for the sensitivity of the x-component of the magnetic field,

$$\frac{\partial H_x(\vec{x}_0)}{\partial \sigma_k} = \int_D \tilde{\vec{E}} \cdot \vec{E} \psi_k(\vec{x}) d\mathrm{v} \tag{10}$$

where the integration is over the region with the perturbed conductivity. For the quarterspace fault model considered in this work (Figure 2a), we consider a region with a uniform conductivity σ_0 and a region beyond the fault boundary corner with a perturbed conductivity $\sigma_0 + \Delta\sigma$ (with coordinates $-\infty < x < \infty,\ y > 0,\ z > 0$). In Eq.(11) we take $k = 1,\ \psi_{k=1}(\vec{x}) \equiv 1,\ \sigma_{k=1} = \sigma_0 + \Delta\sigma$ and rewrite this equation as

$$\frac{\partial H_x(\vec{x}_0)}{\partial \sigma} = \int_D \tilde{\vec{E}}(\vec{x}) \cdot \vec{E}(\vec{x}) \; d\mathrm{v}. \tag{11}$$

Thus, for the calculation of the sensitivity $\partial H_x / \partial \sigma$ in Eq.(11) we need to calculate two electric fields, a primary field $\vec{E}$ and an auxiliary field or *adjoint* field $\tilde{\vec{E}}$, and then integrate their dot product over the region beyond the fault boundary corner where the conductivity is perturbed. For the primary problem we need to compute the electric field $\vec{E}$ produced by a point magnetic dipole source (pointing in some arbitrary orientation) located at the transmitter T of the sonde (Figure 2). For the auxiliary problem we need to

compute the adjoint electric field $\tilde{\vec{E}}$ for a fictitious magnetic dipole source located at the receiver R, and pointing in the direction for which we want to compute the sensitivity of the magnetic field. For Eq.(11) this magnetic dipole would be oriented along the *x*-direction. In general, to compute $\partial H_i/\partial\sigma$, this fictitious magnetic dipole source located at R would point along the *i*th direction, where $i=(x,y,z)$. The sensitivity computed in Eq.(11) is in general, the value of $\partial H_i/\partial\sigma$ measured at the position $\vec{x}_0$ of the receiver R. Once the sensitivity of the magnetic field is computed, we can estimate the value of the magnetic field beyond the fault boundary corner due to a change in the conductivity, to first order in $\Delta\sigma$, as

$$H_i(\vec{x},\sigma)\approx H_i(\vec{x},\sigma_0)+\frac{\partial H_i(\vec{x}_0)}{\partial\sigma}\Delta\sigma. \tag{12}$$

We now want to develop analytic formulas for the electric fields that will be used in the calculation of the sensitivities by means of Eq.(11). In our initial study we began with a code developed for the anisotropic wholespace (Weiss, 2002) in which the region beyond the fault boundary corner had different values for the horizontal and vertical conductivities, $\sigma_h,\sigma_\mathrm{v}$ respectively. Equations for the electric and magnetic fields in the frequency domain produced from a point magnetic dipole source were derived from the work of Moran and Gianzero (1979). However, to test the code and interpret the results, we primarily studied the isotropic case in which $\sigma_h=\sigma_\mathrm{v}\equiv\sigma$. Since one of the goals of this research was to develop a fast running program that could be used for rapid on-site analysis, we decided to develop a code for the isotropic case directly. The isotropic code had the advantage of using much simpler analytic formulas that required much less computation compared to the full anisotropic code. In the following we will discuss the formulas for the electric and magnetic fields produced by a point magnetic dipole for an

isotropic conductivity, and return in Appendix A for a more complete discussion of the anisotropic formulas.

We consider Maxwell's equations with no electric charge or current density $\rho = 0,\ \vec{J}_s = 0$, but a non-zero magnetic current density M_s. Gauss's law then becomes

$$\vec{\nabla} \cdot \vec{E} = 0, \tag{13}$$

which can be exactly satisfied by a electric vector potential $\vec{F}$ such that

$$\vec{E} = -\vec{\nabla} \times \vec{F}. \tag{14}$$

From the remaining Maxwell's equations it can be shown that $\vec{F}$ satisfies the following equation (Ward and Hohmann, 1988)

$$\nabla^2 \vec{F} + k^2 \vec{F} = -i\omega\mu\vec{M}, \tag{15}$$

where ω is the angular frequency of the fields and $\mu = 4\pi \times 10^{-7}$ is the magnetic permeability of free space. For a magnetization $\vec{M}$ for a point magnetic dipole of strength *m* located at the origin and pointing in the *x*-direction $\vec{u}_x$

$$\vec{M} = m\delta(x)\delta(y)\delta(z)\hat{x}, \tag{16}$$

Eq.(15) has the solution

$$\vec{F}(\vec{r}) = \frac{i\omega\mu m}{4\pi r} e^{ikr}\hat{x}. \tag{17}$$

In Eq.(17) k is the complex wavevector given by $k^2 = \mu\varepsilon\omega^2 - i\mu\sigma\omega$ where ε is the dielectric permittivity and $\mu\varepsilon = 1/c^2$ where c is the speed of light. For geological materials at frequencies below 10^5Hz one can assume $\mu\varepsilon\omega^2 << \mu\sigma\omega$ (Ward and Hohmann, 1988) so that the wavevector can be taken as

$$k^2 = -i\mu\sigma\omega, \quad \text{or} \quad k = (1-i)\sqrt{\frac{\mu\sigma\omega}{2}}. \tag{18}$$

By applying Eq.(14) we obtain our expression for the electric field

$$\vec{E} = \frac{i\omega\mu m}{4\pi r^2}\left(ikr+1\right)e^{-ikr}\left(\frac{z}{r}\hat{y} - \frac{y}{r}\hat{z}\right). \tag{19}$$

The above expression for the electric field is utilized in the sensitivity calculation Eq.(11) for both the primary electric field $\vec{E}$ with the point magnetic dipole located at the position of the transmitter T, and for the auxiliary field $\tilde{\vec{E}}$, with the fictitious point magnetic dipole located at the position of the receiver R and pointing in the direction for which component of the magnetic sensitivity will be computed (for e.g. if this fictitious magnetic dipole points in the z-direction then the sensitivity $\partial H_z / \partial\sigma$ is computed in Eq.(11)).

From the spatial dependence e^{ikr} of the electric field in Eq.(19), the complex nature of the wavevector in Eq.(18) implies that $\vec{E}$ will have both oscillatory (Re(k)) and decaying (Im(k)) components. If we define the *skin depth* as

$$\delta = \sqrt{\frac{2}{\omega\mu\sigma}}\ , \tag{20}$$

the electric field can be seen to have a far field spatial dependence that varies essentially as

$$E(r) \sim \frac{e^{-r/\delta}}{r}\cos\left(r/\delta\right)\ . \tag{21}$$

In this work we consider a range of frequencies from 1 to 10^6 Hz. Using $\omega = 2\pi f$ and a representative value of the conductivity $\sigma = 0.25$ S/m, Eq.(20) produces the following values for the skin depth δ

f (Hz)	δ (meters)
20,000	7.1
2000	22.5
200	71.1

which illustrates that the skin depth decreases with increasing ω and σ. Figure 3 illustrates Eq.(21) for the radial dependence of the magnitude of the electric field as a function of skin depth δ for $f = 20,000$ Hz and $\sigma = 0.25$ S/m.

ALGORITHM SUMMARY

To design a code to implement the adjoint method algorithm Eq.(11), for the magnetic field sensitivities $\partial H_i / \partial \sigma$, we first began with a Fortran 77 code (Weiss, 2002) that calculated the electric and magnetic fields for a homogeneous conductivity for an anisotropic wholespace model in the frequency domain (Moran and Gianzero, 1979). The code was modularized and the driver code converted to Fortran 95. We then extended the code to compute the primary $\vec{E}$ and auxiliary electric fields $\tilde{\vec{E}}$ in order to calculate the sensitivities for an anisotropic quarterspace fault model that incorporated different conductivities σ_h, σ_{v} for the horizontal and vertical directions. As discussed earlier, the code was then rewritten and simplified to handle the isotropic case directly. This led to a significant speedup in the overall execution time of the code, and a more direct interpretation of the results.

The integration indicated in Eq.(11) over the three-dimensional region beyond the fault boundary corner was performed with a nested fourth order extended Simpson algorithm. For one dimension the extended Simpson rule for *N* equally spaced points is given by (Press *et al*., 1992)

$$\int_{x_{\min}}^{x_{\max}} f(x)dx = \frac{\Delta x}{3}\left[f_1 + 4 f_2 + 2 f_3 + 4 f_4 + \cdots 2 f_{N-2} + 4 f_{N-1} + f_N \right] + O\left(1/N^4\right) , \qquad (22)$$

which is fourth order accurate. Eq.(22) is no harder to calculate than the second order accurate extended trapezoid or midpoint rule that essentially sums up the function values $f_i = f(x_i)$ at each of the grid points and multiplies by the spacing Δx, and offers the advantage of two more orders of accuracy.

For the integration over the 3D region of the fault boundary corner indicated in Eq.(11), we used a nested set of 1D extended Simpson integrations as illustrated below:

Set $f_x(1:N_x) = 0;\quad f_y(1:N_y) = 0;\quad f_z(1:N_z) = 0$
do $k = 1, N_z$
  do $j = 1, N_y$
    do $i = 1, N_x$
      compute $f\left(x_i, y_j, z_k\right)$ and store in $f_x(i)$
    enddo
    $f_y(j) =$ 1D Simpson integration of $f_x(i)$ values
  enddo
  $f_z(k) =$ 1D Simpson integration of $f_y(j)$ values
enddo
$\iiint f(x,y,z)dxdydz =$ 1D Simpson integration of $f_z(k)$ values

The advantage of nesting 1D integrations is that we only require three 1D arrays f_x, f_y, f_z of lengths N_x, N_y, N_z respectively to store intermediate values, as opposed to one prohibitively large 3D array. For a fixed value of y and z the function values $f\left(x_i, y, z\right)$ are computed along the x-direction and stored in the 1D array f_x. Upon completion of the computation of these function values along a 1D line in the x-direction,

Eq.(22) is used to perform the integral in the y-direction, whose result is stored as an element of the 1D array f_y. After a complete set of function values along a 1D line in the y-direction is computed, Eq.(22) is again invoked to perform integration along the z-direction, whose value is stored as an element of f_z. The net result after cycling through all the x and y grid points is a 1D array f_z that contains the results of the integration of $f(x,y,z)$ over each x-y plane. One more use of Eq.(22) then results in the final integral of $f(x,y,z)$ over the entire region of interest.

The 3D integration over the quarterspace region was computed from the corner of the fault boundary to some arbitrary upper limit. An adaptive integration algorithm was developed to automatically determine the minimum upper limit necessary to produce convergent results. From the Eq.(22), the electric and magnetic fields decay as

$$E, H \sim \frac{e^{-r/\delta}}{r} \qquad \delta = \text{ skin depth } \sim \sqrt{\frac{\rho}{f}},$$

where r is the radial distance from the origin (where the transmitter T is located), $\rho = 1/\sigma$ is the resistivity and f is the frequency in Hertz. Therefore, the upper limit of the quarterspace integration is frequency dependent. Low frequencies fall off as $\sim 1/r$ while high frequencies fall off very rapidly. For frequencies above 10^3 Hz the upper limit of each dimension of the quarterspace integration was initially set to one skin depth. For frequencies below 10^3 Hz, this upper limit was initially set to one-half skin depth, since lower frequencies correspond to a larger spatial region over which the integration had to be performed. After a computation of $\partial H/\partial\sigma$ was performed, the upper limits of the quarterspace region were extended by some fraction of the current skin depth and another calculation of $\partial H/\partial\sigma$ was performed. The computation of the sensitivity $\partial H/\partial\sigma$ was

considered to have converged when the relative error between two successive sensitivity values was less than some user-defined tolerance, set to 10^{-3} in this work. The rough initial approximation of the upper limits of the region of integration, in terms of some number of skin depths, is of practical importance since integration beyond the minimum distance necessary for convergence is computationally expensive, increases run time and adds little to the value of the sensitivity.

The majority of the research presented in this work concerns the magnetic sensitivities computed in the frequency domain. For analyzing the sensitivities in the time domain we incorporated an inverse Fourier sine transform code developed by Hanstein (2003) to compute $\partial H_i(t)/\partial\sigma$,

$$\frac{\partial H_i(t)}{\partial\sigma} = \sqrt{\frac{2}{\pi}}\int_0^\infty \frac{\partial H_i(\omega)}{\partial\sigma}\sin(\omega t)d\omega. \tag{23}$$

In the usual Cooley-Tukey implementation of the Fast Fourier transform (FFT) (Press, 1992) one is required to use equally spaced frequencies. However, the frequency range of the sensitivities span six decades, so this would be impractical. The code developed by Hanstein utilizes a Fast Hankel transform with modified weight coefficients that allows one to use a fixed number of frequencies per decade (either 10 or 15). The right hand side of Eq.(23) is then implemented as

$$\frac{\partial H_i(t)}{\partial\sigma} = \sum_{j=1}^{N} w_j \frac{\partial H_i(\omega_j)}{\partial\sigma}, \tag{24}$$

where the filter coefficients w_j and frequencies ω_j are computed by a least squares fit to known transform pairs, similar to the algorithms described in Anderson (1975) and Guptasarma and Singh (1997) for Hankel transforms. Results of both magnetic sensitivities in both the frequency and time domain are presented in the next section.

SENSITIVITY RESULTS

For the quarterspace fault model (Figure 2a), sensitivities were first calculated for two tool locations, one above and one below the fault boundary in the *y*-*z* plane using the anisotropic code with $\sigma_h = \sigma_v \equiv \sigma$. Receiver locations at 0, 30, 45 and 60 degrees respectively from the vertical *z*-axis were used with a one-meter offset between the transmitter and the receiver (Figure 2b). For these cases, we used the adjoint method by calculating $\vec{E}$ with a *z*-magnetic directed dipole at the transmitter and $\tilde{\vec{E}}$ with a *x*-directed magnetic dipole at the receiver.

Figure 4 shows the frequency domain sensitivity plots (a) above and (b) below the fault boundary corner. The absolute values of the sensitivities were plotted for 34 frequencies from 1 Hz to 1 MHz. We find that for various tool locations the values of sensitivities peak around 100 kHz, and approach zero for very low or very high frequencies. Peak values are maximum for vertical receiver positions (along the *z*-axis), and decrease, as the receiver is oriented more horizontally (along the *y*-axis) for both the above and below cases due to the fact that the transmitter position for the below case was only one meter below the fault boundary corner.

Figure 5 shows the time domain sensitivity plots (a) above and (b) below the fault boundary corner over a dynamic range of four decades of the instrument strength. The cusps at $t < 20$ μs indicate a sign change in $\partial H / \partial \sigma$. Note that the magnitude of the perturbation covers four decades in signal strength. Note, also, that the effect of the quarterspace is more clearly discerned in the frequency domain (Figure 4) as the magnitude of the peak amplitudes.

In Figures 6 and 7, the absolute values of the sensitivities were calculated for the

frequency and time domain for tool locations around the fault boundary corner from zero to 20 meters, in five-meter intervals in the *y*-*z* plane. Receiver locations at 0, 30, 45, 60 and 90 degrees respectively from the vertical *z*-axis were used with a one-meter offset between the transmitter and the receiver. For these cases, we used the adjoint method by calculating a magnetic dipole at the transmitter in the direction of the receiver and an *x*-directed magnetic dipole at the receiver.

In the frequency domain sensitivity plots illustrated in Figure 6, we show three representative plots of the sensitivities around the fault boundary corner at a five-meter distance. We again find that the values of sensitivities for the five tool locations peak around 100 kHz around the fault boundary corner, and approach zero for very low or very high frequencies. A symmetry of response can be seen in these sensitivity plots. In the upper right quadrant, the peak values of the sensitivities for each tool location increased as the sonde was rotated more towards the vertical (i.e. *z*-axis), whereas in the lower left quadrant, the peak values of the sensitivities for each tool location increased as the sonde was rotated more towards the horizontal (i.e. *y*-axis).

The time domain sensitivity plots (Figure 7) around the fault boundary corner show a dynamic range of five decades of the instrument strength. The cusps (or zero crossings) at t <20 ms indicate a sign change in $\partial H/\partial\sigma$. A symmetry of response can also be seen in the time domain sensitivity plots. Figure 8 illustrates the frequency and time domain plots relative to the fault boundary corner.

In the frequency domain sensitivity plots in Figure 9, we calculate the absolute value of $\partial H/\partial\sigma$ for various $(\Delta y, \Delta z)$ pairs over the region of the model from zero to 20 meters in the *y*-*z* plane, in five-meter intervals around the fault boundary corner for tool locations

at θ = 0˚, 45˚, and 90˚. Note the symmetry of response for the various tool locations. For the (a) vertical sonde (θ = 0˚), the peak values of the sensitivities decrease as the sonde is parallel to the *z*-axis of the fault boundary corner, whereas for (c) the horizontal sonde (θ = 90˚), the peak values of the sensitivities decrease, as the sonde is parallel to the *y*-axis of the fault boundary corner.

In the time domain sensitivity plots in Figures 10, we also calculate $\partial H/\partial\sigma(t)$ for various $(\Delta y, \Delta z)$ pairs over the region of the model from zero to 20 meters, in five-meter intervals around the fault boundary corner, but for tool locations at θ = 0˚, 30˚, and 45˚. The magnetic field sensitivity was calculated for 21 time steps, three early time points are shown here. The same symmetry of response seen in the frequency domain around the fault boundary corner is also evident in the time domain. The cusps (or zero crossings) can clearly be seen in Figure 10b for θ = 0˚, at t = 2.512 e-05 and for all tool locations in Figure 10c at t = 3.981 e-05.

We then used two tool location cases (Figure 11) for the next set of runs: (11a) tool 1 using the adjoint method by calculating a magnetic dipole at the transmitter and receiver in the direction of the tool orientation and (11b) tool 2, using the adjoint method by calculating a magnetic dipole at the transmitter in the direction of the receiver and an *y or z*-directed magnetic dipole at the receiver. In this case the *x,y,z* coordinates of the receiver dipoles follow the absolute *x,y,z* coordinates of the fault boundary corner.

In Figures 12 through 16, the absolute values of the sensitivities were calculated for the frequency domain for tool locations around the fault boundary corner from zero to 20 meters, with a higher resolution of one-meter intervals in the *y-z* plane. To calculate these 1281 points, we switched to a purely isotropic code, in which the analytic formulas were

much simpler and which ran faster. Receiver locations at 0, 22.5, 45, 67.5 and 90 degrees respectively from the vertical *z*-axis were used with a one-meter offset between the transmitter and the receiver. Also, because of the one-meter offset between the transmitter and the receiver, we can only show sensitivities within one meter of the fault corner boundary. Closer measurements would place the receiver inside the area of perturbed conductivity.

Figure 12 shows the higher resolution runs in the frequency domain for tool 1, transmitter and receiver dipole in the direction of the tool orientation for frequency = 20,000 Hz and a wholespace conductivity = 0.25 S/m, for (a) the vertical sonde (θ= 0˚), (b) the sonde dipping at 22.5˚(θ= 22.5˚), (c) 45˚(θ= 45˚), (d) 67.5˚(θ= 67.5˚), and (e) the horizontal sonde (θ = 90˚). Note again the similar symmetry of response as in the lower resolution figures in the frequency domain of Figure 9 for (a) the vertical sonde (θ = 0˚), the peak values of the sensitivities decrease as the sonde is parallel to the *z*-axis of the fault boundary corner, whereas for (e) the horizontal sonde (θ = 90˚), the peak values of the sensitivities decrease, as the sonde is parallel to the *y*-axis of the fault block.

For the second tool location, tool 2, where the transmitter dipole is in the direction of the tool orientation and the receiver dipole in the *y*-direction with Frequency = 20,000 Hz, wholespace conductivity = 0.25 S/m, Figure 13 illustrates (a) the vertical sonde (θ= 0˚), (b) the sonde dipping at 45˚(θ= 45˚), and (b) the horizontal sonde (θ = 90˚). Note in (a) when the transmitter and receiver dipoles are 90° apart (i.e. when the transmitter dipole in the direction of the tool orientation, (θ= 0˚) and the receiver dipole in the *y*-direction) we observe a magnitude asymmetry that has a “keyhole” like appearance. In Figure 14c, we observe this feature again when the transmitter dipole is in the direction of

the tool orientation (θ = 90˚) and the receiver dipole is in the z-direction. We will further discuss this feature in the next section.

Figure 15 and 16 show the higher resolution runs in the frequency domain for tool 1, transmitter and receiver dipole in the direction of the tool orientation, wholespace conductivity = 0.25 S/m, for frequency = 2000 Hz and frequency = 200 Hz. Note the similar symmetry characteristics of Figure 12 at frequency 20,000 Hz.

INTERPRETATION OF SENSITIVITIES

Some of the features observed in the preceding section for the sensitivities $\partial H_i(\omega)/\partial\sigma$ in the frequency domain can be explained by examining the angular dependence of the primary and auxiliary fields in computing the 3D integral over the fault boundary corner in Eq.(11). The equation for the electric field $\vec{E}$ in Eq.(19) was derived for the specific case of a point magnetic dipole pointing along the x-direction. We note that $\vec{E}$ has no component along the x-direction itself, which reflects the well-known fact that "figure eight" radiation pattern from a dipole source is oriented perpendicular to direction of the dipole. The remaining non-zero components of this particular $\vec{E}$ have the form $\vec{E}^{m_x} \sim (0, z/r, -y/r)$, where the added superscript on the electric field is meant to indicate that this electric field results from a magnetic dipole pointing along the x-direction, and the 3-vector indicates the field components along the x, y and z directions. Using spherical coordinates $x = r\sin\theta\cos\phi$, $y = r\sin\theta\sin\phi$, $z = r\cos\theta$ where θ is the polar angle measured from the positive z-axis and ϕ is the azimuthal angle measured from the positive x-axis (see Figure 17), the angular dependence of $\vec{E}^{m_x}$ is given by $\vec{E}^{m_x} \sim (0, \cos\theta, -\sin\theta\sin\phi)$. Since the electric field was derived from the curl of the

electric vector potential $\vec{E} = -\vec{\nabla} \times \vec{F}$, we can easily infer the angular dependence of the electric fields for point magnetic dipole sources oriented along the *y* and *z* directions:

$$\begin{aligned}
&\vec{E}^{m_x} \sim (0, z/r, -y/r) = (0, \cos\theta, -\sin\theta\sin\phi) && \text{for dipole } \vec{M} = m\delta(\vec{x} - \vec{x}_0)\vec{u}_x, \\
&\vec{E}^{m_y} \sim (-z/r, 0, x/r) = (-\cos\theta, 0, \sin\theta\cos\phi) && \text{for dipole } \vec{M} = m\delta(\vec{x} - \vec{x}_0)\vec{u}_y, \quad (25) \\
&\vec{E}^{m_z} \sim (y/r, -x/r, 0) = (\sin\theta\sin\phi, -\cos\theta\sin\phi, 0) && \text{for dipole } \vec{M} = m\delta(\vec{x} - \vec{x}_0)\vec{u}_z.
\end{aligned}$$

The integrand of Eq.(11) involves the dot product of the primary and auxiliary electric fields $\vec{E}$ and $\tilde{\vec{E}}$ integrated over the fault boundary corner

$$\frac{\partial H_x(\vec{x}_0)}{\partial \sigma} = \int_D \vec{E}(\vec{x}) \cdot \tilde{\vec{E}}(\vec{x})\, dv = \int_{r_{min}}^{\infty} dr\, r^2 \int_0^{\theta_{max}} d\theta\ \sin^2\theta \int_0^{\pi} d\phi\ \vec{E}_T(\vec{x}) \cdot \tilde{\vec{E}}_R(\vec{x}), \qquad (26)$$

where we have rewritten the integration over the domain *D* in terms of spherical coordinates, and added a subscript T and R to the fields $\vec{E}$ and $\tilde{\vec{E}}$ respectively, to indicate the location of the magnetic dipole source associated with each field. The limits of integration of the domain *D*, the quarterspace region beyond the fault boundary corner, are given by

$$-\infty < x < \infty,\ 0 < y_{min} \le y < \infty,\ 0 < z_{min} \le z < \infty,$$

where $(0, y_{min}, z_{min})$ is the position of the origin of the fault boundary corner, in the *y*-*z* plane, relative to the transmitter. From Figure 17 we observe that the integration over *x* is equivalent to an integration over the azimuthal angle ϕ from 0 to π.

Consider the case of tool 1 in which the sonde is oriented in the *y*-*z* plane at some angle θ, and transmitter dipole is directed along the sonde. Since Maxwell's equations are linear, so that the fields add, the electric field $\vec{E}_T$ produced from this dipole orientation is the sum of the electric fields from a dipole oriented along the *y*-direction and a dipole oriented along the *z*-direction, which we label as $\vec{E}_T^{\theta} = \sin\theta\ \vec{E}_T^{m_y} + \cos\theta\ \vec{E}_T^{m_z}$.

In addition, let us also consider a dipole located at the receiver R and pointing in the *x*-direction that we label as $\tilde{\vec{E}}_R = \tilde{\vec{E}}_R^{m_x}$. For the computation of $\partial H_x / \partial \sigma$, an inspection of the angular dependences of the fields in Eq.(25) reveals that the integrand $\vec{E}_T^{\theta} \cdot \tilde{\vec{E}}_R = \left(\sin\theta \;\; \vec{E}_T^{m_y} + \cos\theta \;\; \vec{E}_T^{m_z}\right) \cdot \tilde{\vec{E}}_R^{m_x}$ of Eq.(26) has angular dependence that varies as $\sin\phi\cos\phi = 1/2\sin 2\phi$ for the $\vec{E}_T^{m_y} \cdot \tilde{\vec{E}}_R^{m_x}$ term and as $\sin\phi$ for the $\vec{E}_T^{m_z} \cdot \tilde{\vec{E}}_R^{m_x}$ term. However, the integration of these functions over the range $\int_0^{\pi} d\phi$ yields exactly zero. Thus we conclude that $\partial H_x / \partial \sigma \equiv 0$, as is computed numerically from the code. In Figure 18 we show the Re and Im parts of the integrand $\vec{E}_T^{\theta}(\vec{x}) \cdot \tilde{\vec{E}}_R(\vec{x})$ for angles $\theta = (0°, 45°, 90°)$. We see that each plot is symmetric about zero, and therefore all positive contributions to the integrand exactly cancel with the negative contributions. In the numerical code, we obtain sensitivities with magnitudes $\approx 10^{-21}$. For a receiver dipole oriented along the *y* or *z* directions the integrand will pick up azimuthal terms such as $\cos^2\phi = 1/2\left(1 + \cos 2\phi\right)$ and $\sin^2\phi = 1/2\left(1 - \cos 2\phi\right)$ that produce non-zero contributions when integrated over $\int_0^{\pi} d\phi$. Thus, the previous symmetry argument cannot be used to conclude much about these other orientations.

Having discussed the symmetry related to the angle ϕ, we now consider features of the sensitivities associated with the polar angle θ. In several of the *y*-*z* plane sensitivity plots presented earlier we observe an asymmetry in the magnitude of $\partial H_i / \partial \sigma$ depending on whether *y*>0 and *z*<0, or *y*<0 and *z*>0. Figure 19a illustrates such a magnitude asymmetry that has a "keyhole" like appearance. This feature can be explained by examining the integrand in Eq.(26) with respect to the angle θ.

From Figure 19 and Eq.(26) we observe that the upper limit $\theta_{\max}$ in the integral over the angle θ, which is measured from the positive *z*-axis, depends on the relative position of the fault boundary corner in relation to the location of the transmitter T (the origin of coordinates, $\vec{x}=0$). If T lies above the fault boundary corner as illustrated in Figure 19b, then $\theta_{\max}=\pi/2$. However, if T lies below the fault boundary corner as shown in Figure 19c, the maximum polar angle lies somewhere in the range $\pi/2 \le \theta_{\max} < \pi$.

When the transmitter is above the fault boundary corner $(0 \le \theta \le \pi/2)$ the integration over the functions $\sin\theta$ and $\cos\theta$ appearing in the integrand (which are greater than zero in this range), produces only positive contributions. However, when the transmitter is below the fault boundary corner $(0 \le \theta \le \theta_{\max} < \pi)$, integrands containing $\cos\theta$ (which is negative for $\theta > \pi/2$) can produce negative contributions, which can partially cancel the positive contributions coming from the portion of integration over the range $0 \le \theta \le \pi/2$. Since $\theta_{\max}$ never reaches π (corresponding to the origin of fault boundary corner located at $z=-\infty$) these negative contributions can never exactly cancel the positive contributions, as occurred in the integration over ϕ for an *x*-directed receiver dipole as discussed above. In fact, the larger the negative value of the *z*-coordinate of the fault boundary corner as shown in Figure 19c, the larger the value of $\theta_{\max}$, and thus the greater the cancellation between positive and negative contributions of the integrand, leading to a smaller value for the magnitude of the sensitivity (see the region *y*>0 and *z*<0 in Figure 19a). This explains the asymmetric "keyhole" feature seen in many of the 2D *y*-*z* sensitivity plots.

As a final symmetry consideration, we note that for the case of the T and R dipoles oriented in the *same* direction as illustrated in Figure 20a, the integrand of Eq.(26) is

approximately $\vec{E}_T \cdot \tilde{\vec{E}}_R \approx \left|\vec{E}_T\right|^2$ as long as r is much greater than the offset between T and R, which is one meter in this study. Under these conditions the integrand is nearly always positive, and therefore cancellations that can arise from the integration over the angles θ and ϕ hardly occur. Therefore, the magnitude of the sensitivities should be largest for this parallel dipole case, and this is what is observed numerically. It should be noted that for the parallel dipole case, cancellations in the integrand $\vec{E}_T \cdot \tilde{\vec{E}}_R$ can and do occur when the fault boundary corner is close to the transmitter, since then angles θ_T, ϕ_T associated T and the angles θ_R, ϕ_R as associated with R for a field point in the quarterspace region are not quite the same. But as we integrate deeper into the quarterspace region, these angles become nearly identical and any possible cancellations become negligible. The result we see is that parallel dipole orientations at T and R produce the strongest magnitude sensitivities.

The overall magnitude of the sensitivities can be addressed as we vary the frequency ω. From Figure 21, where all the *y-z* plane sensitivity plots are shown on the same colorbar scale, we see that the strongest magnitude sensitivities occur for the larger frequencies. This results from Eq.(19) where the magnitude of the electric field $\vec{E}$ is seen to be proportional to $\omega = 2\pi f$. Thus the integrand $\vec{E}_T \cdot \tilde{\vec{E}}_R$ in Eq.(26) for computing $\partial H_i / \partial \sigma$ scales as ω^2. In Figure 21 we plot the magnitude of $\partial H / \partial \sigma$ for f = (2 x10^4, 2 x10^3, 2 x10^2) Hz and observe the peak intensities drop off by a factor of 10^2 for each successive decrease of the frequency by a factor of 10.

We can obtain more information about the frequency dependence of the magnitude of sensitivities by plotting the real and imaginary parts of $\partial H_i / \partial \sigma$. In Figures 22-25 the real

and imaginary parts of the sensitivities are plotted for 90 frequencies from 1 Hz to 1 MHz. On a loglog plot, each of these curves show similar behavior of (1) a linear dependence of the $\mathrm{Re}\left|\partial H_i/\partial\sigma\right|$ and $\mathrm{Im}\left|\partial H_i/\partial\sigma\right|$ for frequencies below ~10^4 Hz and (2) an oscillatory behavior for frequencies above ~10^4 Hz. We can understand these behaviors as follows. From Eq.(19) the electric field amplitude varies as $E(r) \sim \omega(ikr+1)e^{-ikr}$ where the complex wavevector k is given by Eq.(18) $k = (1-i)\sqrt{\mu\sigma\omega/2} \equiv (1-i)/\delta$, with δ the skin depth. Thus the oscillatory part of the sensitivity varies as $\exp\left(-i\sqrt{\mu\sigma\omega/2}r\right)$. For small frequencies, this factor is essentially one since the magnetic permittivity has a numerical value of $\mu = 4\pi\times10^{-7}$. As discussed above, the integrand $\vec{E}_T\cdot\tilde{\vec{E}}_R$ of Eq.(26) scales as ω^2. On the loglog plots of Figures 22-25 the slope of the linear portion of the graphs is roughly 2 as it would be for an ω^2 dependence (with any deviation from the exact value of 2 coming from the other factors of k that appear in the integrand). For higher frequencies, we note that $\sqrt{\mu\sigma\omega/2}$ becomes on the order of one for frequencies ~10^4 Hz (using a value of $\sigma = 1$). Above this frequency, the factor

$$\exp\left(-i\sqrt{\mu\sigma\omega/2}r\right) = \cos\left(\sqrt{\mu\sigma\omega/2}r\right) - i\sin\left(\sqrt{\mu\sigma\omega/2}r\right)$$

begins to exhibit oscillations as shown in Figures 22-25. The cusps in the oscillations are due to the fact that we are plotting the absolute value of the sensitivities (since we are using a loglog plot for the large range of values 10^{-15} – 10^{-6} that they exhibit).

This dependence of the sensitivities on the frequency in the form of the factor $\sqrt{\mu\sigma\omega/2}$ is further justified when we note that a change of the conductivity σ by a factor of four in going from Figure 22a to Figure 22c produces *twice* as many oscillations. From Eq.(26) $\partial H_i/\partial\sigma$ depends on the integration of $\vec{E}_T\cdot\tilde{\vec{E}}_R$ over the fault

boundary corner, so that there is no spatial dependence remaining. When we write that $\partial H_i/\partial\sigma$ varies as $\exp\left(-i2\sqrt{\mu\sigma\omega/2}r\right)$ (the extra factor of two coming from the product of the electric fields $\vec{E}_T\cdot\tilde{\vec{E}}_R$ in the integrand) we can interpret r as some characteristic distance, which can be taken as the distance to the fault boundary corner. In Figure 22a and Figures 23a-c, $r=5\sqrt{2}$ meters. In Figure 24, the distance to the fault boundary corner has been doubled to $r=10\sqrt{2}$ meters, and exhibits *twice* as many oscillations as the previous graphs. Thus we conclude that the real and imaginary parts of the sensitivities vary with frequency approximately as

$$\left|\partial H_i/\partial\sigma\right| \sim \omega^2 \exp\left(-i2\sqrt{\mu\sigma\omega/2}r_{fbc}\right), \tag{27}$$

where r_{fbc} is the distance to the fault boundary corner. Finally, in Figure 25 we show the real and imaginary parts of the sensitivities vs. frequency for various tool locations. Though there are slight differences in the magnitudes of the graphs, the overall features are essentially the same, as discussed above.

Plotting the Integrand

In Figures 27 – 31, we plot the integrand $\vec{E}_T(\vec{x})\cdot\tilde{\vec{E}}_R(\vec{x})$ of Eq.(9) in the *y-z* plane for three tool orientations as shown in Figure 26 for 20,000Hz. Figure 26 shows the orientation of tool 1 (transmitter and receiver dipole in the direction of the tool orientation), for the sonde (1) above (vertical $\theta=0°$), (2) dipping at $\theta=45°$ above and to the right, and (3) the horizontal and below, the fault boundary corner. Figures 27-29 plot the real, imaginary and absolute value of the integrand for $\theta=(0°,45°,90°)$ and position of the fault boundary corner of $\vec{x}=(0,-5,5)$, $\vec{x}=(0,5,5)$, $\vec{x}=(0,5,-5)$ meters, respectively.

The vertical and horizontal sonde show a characteristic two-peaked feature, with both peaks having the same sign. The position of the peaks are mirror images of each other through the line $y=z$. The sonde dipping at $\theta = 45°$ shows a more symmetrical single peaked feature, centered about the diagonal line $y=z$.

In Figure 30 we show the absolute value of the integrand for $\theta = (0°, 45°, 90°)$. It appears that as we rotate the sonde from zero to ninety degrees, the double peaked feature at 0˚ (Figure 30a) merges into the single peaked feature at 45˚ (Figure 30b) and then separates into a mirrored image double peak feature again at 90˚. From these figures we note that the peaks are separated by roughly the radial distance to the fault boundary corner, which is $r_{fbc} = 5\sqrt{2}$ meters for this case. In Figure 31 we show the vertical sonde at $\vec{x} = (0, -5, 5)$ in (a) and $\vec{x} = (0, -10, 10)$ in (b) corresponding to $r_{fbc} = 5\sqrt{2}$ and $r_{fbc} = 10\sqrt{2}$ respectively. We observe that in Figure 31b, the peaks are twice as far apart ($\approx 10\sqrt{2}$ meters) as in Figure 31a ($\approx 5\sqrt{2}$ meters). This might possibly be related to Eq.(27) above which for fixed frequency ω and conductivity σ has an oscillation proportional to r_{fbc}.

Sensitivities in Oblique Planes

So far in this study, we have only investigated the sensitivities in the *y-z* plane (or perpendicular to the fault boundary corner). In this section we investigate the sensitivities in oblique planes around the fault corner boundary. Figure 32 shows a map projection of the fault boundary corner. Sensitivities in the oblique planes around the fault boundary corner were calculated in the *x-z* plane (ϕ = 0˚), angled at 22.5˚ (ϕ= 22.5˚), 45˚ (ϕ= 45˚), 67.5˚ (ϕ= 67.5˚), and in the *y-z* plane, (ϕ = 90˚).

We used two tool location cases (Figure 33) for the next set of runs: (33a) tool 1 using the adjoint method by calculating a magnetic dipole at the transmitter and receiver in the direction of the tool orientation and (33b) tool 2 for these runs, using the adjoint method by calculating a magnetic dipole at the transmitter in the direction of the receiver and an *x, y or z*-directed magnetic dipole at the receiver. In Figures 34 through 37 the orientation of the dipole at the receiver (*x,y,z* directions) are *relative* to the *sonde axis*.

In Figures 34 through 38, the absolute values of the sensitivities were calculated for oblique planes in the frequency domain for tool locations around the fault boundary corner from zero to 20 meters, with a resolution of one-meter. Receiver locations at 0, 22.5, 45, 67.5 and 90 degrees respectively from the vertical *z*-axis were used with a one-meter offset between the transmitter and the receiver. We used frequency = 20,000 Hz, and wholespace conductivity = 0.25 S/m. Again, due to the one-meter offset between the transmitter and the receiver, we can only show sensitivities within one meter of the fault corner boundary to avoid placing the receiver inside the area of perturbed conductivity.

In Figure 34, the sensitivities were plotted for tool 1, transmitter dipole and receiver dipole in the direction of the sonde for the horizontal sonde in the (a) *x-z* plane, (b) angled at 22.5˚ (ϕ= 22.5˚), (c) 45˚ (ϕ= 45˚), (d) 67.5 ˚ (ϕ= 67.5˚), and (e) 90˚ (ϕ = 90˚). Note that as the horizontal sonde is rotated from the *y-z* plane (ϕ = 90˚) to the *x-z* plane (ϕ= 0˚), the value of the sensitivities are similar until the sonde is rotated parallel to the fault boundary corner in the *x-z* plane where we see a marked decrease in the values.

In Figure 35, we plot the sensitivities for tool 1, with the transmitter and receiver dipole in the direction of the sonde, in the oblique plane angled at ϕ= 45˚ for (a) the vertical sonde (θ= 0˚), (b) the sonde dipping at 22.5˚(θ= 22.5˚), (c) 45˚(θ= 45˚), (d)

67.5˚(θ= 67.5˚), and (e) the horizontal sonde (θ = 90˚). The main point to note in these oblique-plane sensitivity plots is that they are qualitatively similar to each other, regardless the value of θ.

Figure 36 shows the sensitivities in the oblique planes around the fault boundary corner for tool 2 using a magnetic dipole at the transmitter in the direction of the receiver and an *x*-directed magnetic dipole at the receiver for the horizontal sonde in (a) the *x*-*z* plane (ϕ = 0˚), angled at (b) 22.5˚ (ϕ= 22.5˚), (c) 45˚ (ϕ= 45˚), (d) 67.5˚ (ϕ= 67.5˚), and (e) in the *y*-*z* plane (ϕ = 90˚). As the sonde rotates from the *x*-*z* plane to the *y*-*z* plane, we see that the sensitivities increase until they reach a maximum at ϕ= 45˚ and then decrease until they approach zero in the *y*-*z* plane. We would expect these values to gradually decrease from ϕ= 45˚ to ϕ = 90˚, but instead we see an abrupt cut off at the ϕ = 90˚. To investigate this further, we calculated the sensitivities in the oblique planes in one degree intervals around the fault boundary corner (Figure 37) for the horizontal sonde angled at (a) 87˚ (ϕ = 87˚), (b) 88˚ (ϕ = 88˚), (c) 89˚ (ϕ = 89˚) from the *x*-*z* plane, and (d) in the *y*-*z* plane, 90˚ (ϕ = 90˚). As the sonde rotates to the *y*-*z* plane, we see the sensitivity values decrease, but again we see them abruptly cut off at ϕ = 90˚. This implies that the sonde is very sensitive to the fault when the sonde is perpendicular to the fault, but that the fault boundary corner cannot be easily detected when the sonde is positioned in any of the oblique planes. Recall that in the numerical code, the spatial resolution (dx, dy, dz) was one meter (the distance between the transmitter and the receiver). Increased resolution might possibly reveal a more gradual decrease in the sensitivities as ϕ approaches 90˚. However, this would increase the execution time of the code, which impedes the goal of developing a fast running code for rapid on-site analysis of induction log data.

In Figure 38 we show the sensitivities for the horizontal sonde parallel to the fault boundary corner (i.e. the *x*-*z* plane) with the receiver dipole in the (a) *x*-direction, (b) *y*-direction, and (c) in the *z*-direction. We see a "keyhole" feature for an x-directed and z-directed receiver dipole (though slightly more diffused), similar to what was observed in the *y*-*z* plane and was discussed above in the Interpretation of Sensitivities section. As in the *y*-*z* plane, we observe this feature when the transmitter dipole is in the direction of the tool orientation ($\theta = 90°$) and the receiver dipole is perpendicular to the transmitter dipole, Figure 19a. The new feature here is that the *x*-directed receiver dipole sensitivity plot Figure 38a, is non-zero in the oblique plane, where it was exactly zero in the *y*-*z* plane. For $\phi = 0$, parallel to the fault boundary corner, both the *x*-directed and *z*-directed receiver dipoles produce "keyhole" features.

CONCLUSIONS

By modeling electromagnetic induction with the adjoint method, we are able to quickly interrogate various geologic models with non-uniform conductivities. With this method we are able to obtain good values of the sensitivities $\partial H_i(\omega)/\partial\sigma$. We find that we do not need to integrate very far into region beyond the fault boundary as the fields fall off rapidly and the sensitivity estimates converge very quickly.

The numerical investigations discussed in this work were designed to address the questions of optimal drilling strategy and tool orientation for detection of an isolated fault block (i.e. *rules of thumb* for drilling around a fault block). From the results of this study we have found the following:

1) The absolute values of the sensitivities plotted in the frequency domain for 1 Hz

to 1 Mhz show that for various tool locations the values of sensitivities peak around 100 kHz, and approach zero for very low or very high frequencies.

2) In the time domain the magnitude of the perturbation covers four decades in signal strength for tool locations out to 20 meters from the fault boundary corner.
3) In the frequency domain the effect of the quarterspace is more clearly discerned as the magnitude of the peak amplitudes.
4) The results demonstrate in the frequency and time domain that a vertical sonde is most sensitive to the fault block when it approaches above rather than parallel to the side. A horizontal sonde is most sensitive to the fault block when it approaches to the side rather than above the fault block.
5) Some of the features observed for the sensitivities in the frequency domain can be explained by examining the angular dependence of the primary and auxiliary fields in computing the 3D integral over the fault boundary corner.
    a. The ”Keyhole” feature. For the case when transmitter and receiver dipoles are 90° apart, this feature can be explained by the relative position (above/below) of the transmitter to the fault boundary corner.
    b. The strongest magnitude of the sensitivities occurs when the transmitter and receiver dipoles are in the same direction. The weakest magnitudes occur when the transmitter and receiver dipoles are 90° apart.
    c. Overall magnitude of the sensitivities can be addressed as we vary the frequency. We observe the strongest magnitude sensitivities occur for the larger frequencies, which results from the linear dependence of the electric field amplitude on the frequency.

6) We can obtain more information about the frequency dependence of the magnitude of sensitivities by plotting the real and imaginary parts of $\partial H_i / \partial \sigma$.

   a. We find a linear dependence of the real and imaginary parts for frequencies below ~10^4 Hz and an oscillatory behavior for frequencies above ~10^4 Hz.

   b. A change of the conductivity σ by a factor of four from 0.25 S/m to 1.00 S/m produces twice as many oscillations above ~10^4 Hz.

   c. When the distance to the fault boundary corner is doubled, the real and imaginary parts of the sensitivities also exhibit twice as many oscillations.

   d. The above results can be explained by a consideration of the dependence of the fault boundary corner skin depth on frequency and conductivity.

7) Sensitivities in oblique planes around the fault corner boundary show similar symmetry of response for the various tool locations as in the plane perpendicular to the fault boundary corner (the *y*-*z* plane).

8) For tool 1 (with the transmitter and receiver dipole in the direction of the sonde), we find that as the horizontal sonde is rotated obliquely away from the (perpendicular) *y*-*z* plane, the value of the sensitivities are similar until the sonde is parallel to the fault boundary corner (the *x*-*z* plane) where we see a marked decrease in the sensitivity values.

9) For tool 2 (with the magnetic dipole at the transmitter in the direction of the receiver and an *x*-directed magnetic dipole at the receiver), we find that the horizontal sonde is very sensitive to the fault boundary corner when the sonde is oriented perpendicular to it. However, the fault boundary corner is not as easily

detected when the sonde (regardless of orientation) is positioned in any of the oblique planes.

In this study we have purposely considered a simple quarterspace model containing a single region of perturbed conductivity in order to test the adjoint method and interpret the forward model results. Our goal was to develop an analytic approach for rapid on-site analysis of induction log data, which could be applied to geologic materials with inhomogeneous conductivities. The work presented in this study forms a basis from which further worthwhile avenues of investigations can be explored, including: (1) comparing sensitivities computed with the adjoint method with 3D finite difference results to determine the range of the change of conductivity; (2) calculating sensitivities for the anisotropic case (vertical conductivity does not equal the horizontal conductivity); (3) calculating sensitivities for cases with multiple non-interacting regions of different conductivities; (4) calculating higher order derivatives in the Taylor series expansion using the adjoint method and (5) investigating models with fluids in the fault zone.

BIBLIOGRAPHY

Anderson, B.I., 2001, Modeling and Inversion Methods for the Interpretation of Resistivity Login Tool Response, Delft University Press, 378 p.

Anderson, W.L., 1975, Improved digital filters for evaluation Fourier and Hankel transform integrals, USGS Report No. USGS-GD-75-012.

Anderson, B.I, Barber, T.D., and M.G. Luling, 1995, The response of induction tools to dipping, anisotropic formations in SPWLA 36th Annual Logging Symposium Transactions, Society of Profession Well Log Analysts, Paper D.

Anderson, B., and S. Gianzero, 1983, Induction sonde response in stratified media, *The Log Analyst*, v. 24, p. 25-31.

Anderson, B.I., Safinya, K.A., and T. Habashy, 1986, Effects of dipping beds on he response of induction tools in *Proceedings 1986 SPE Annual Technical Conference and Exhibition*. Society of Petroleum Engineers, Paper SPE 15488.

Archie, G.E., 1942, The electric resistivity log as an aid in determining some reservoir characteristics, Trans. AIME 146, p. 54-62.

Doll, H.G., 1949, Introduction to induction logging and application to logging of wells drilled with oil base mud, *Journal of Petroleum Technology*, v1, p. 149-162.

Dyck, A.V, 1988, Drill-hole electromagnetic methods in Electromagnetic Methods in Applied Geophysics, ed. M.N. Nabighian, Society of Exploration Geophysics, Tulsa, Oklahoma, 513 p.

Guptasarma, D., and B. Singh, 1997, New digital linear filters for Hankel and J_0 and J_1 transforms, Geophys. Prosp., v 45, p. 745-762.

Hanstein, T., 2003, private communication and contributed code.

Moran, J.H., and Gianzero, S., 1979, Effects of formation anisotropy on resistivity-logging measurements, *Geophysics*, v. 44, p. 1266-1286.

Moran, J.H., and Kunz, K.S., 1962, Basic theory of induction logging: and application to study of two-coil sondes, *Geophysics*, v. 27, p. 829-858.

McGillivray, P.R., D.W. Oldenburg, R.G. Ellis and Habashy, T.M., 1994, Calculation of sensitivities for the frequency domain electromagnetic problem, *Geophysical Journal International*, v. 116, p. 1-4.

Press, W.H., Teukolsky, S.A., Vettering, W.T., and Flannery, B.P., 1992, Numerical Recipes in Fortran, 2 ed., Cambridge University Press, 963 p.

Telford, W.M., Geldart, L.P., and R.E. Sheriff, 1990, Applied Geophysics, 2nd Ed., Cambridge University Press, 770 p.

Ward, S.H., and G.W. Hohmann, 1988, Electromagnetic theory for geophysical applications in Electromagnetic Methods in Applied Geophysics, ed. M.N. Nabighian, Society of Exploration Geophysics, Tulsa, Oklahoma, 513 p.

Weiss, C.J., 2002, private communication and contributed code.

Weiss, C.J., and Newman, G.A., 2002, Electromagnetic induction in a fully 3-D anisotropic earth, Geophysics, v.67, no. 4, p. 1104 – 1114.

Weiss, C.J., and Newman, G.A., 2003, Electromagnetic induction in a generalized 3-D anisotropic earth, Part 2: The LIN preconditioner, Geophysics, v.68, p. 992 - 930.

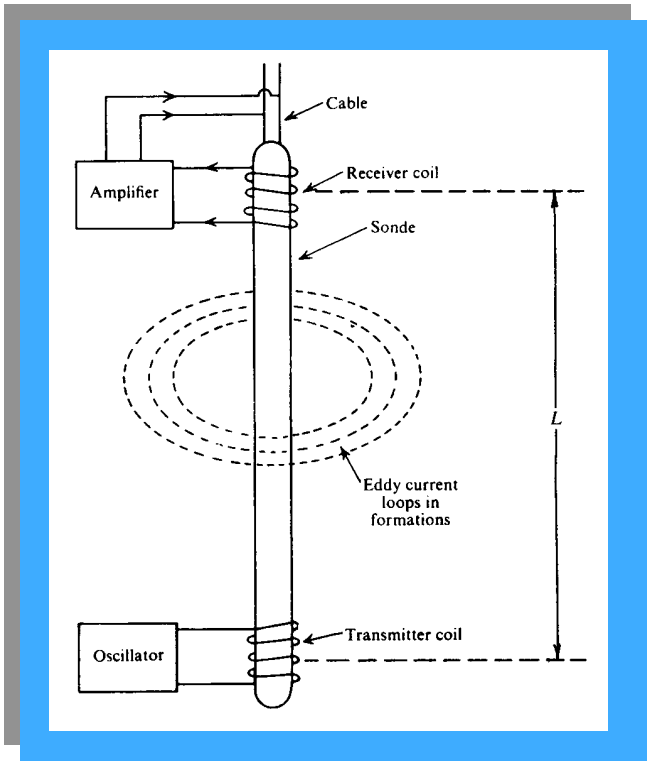

Figure 1: An induction sonde consisting of a transmitter and a receiver, designed to measure formation resistivity in boreholes (Telford *et al*., 1990).

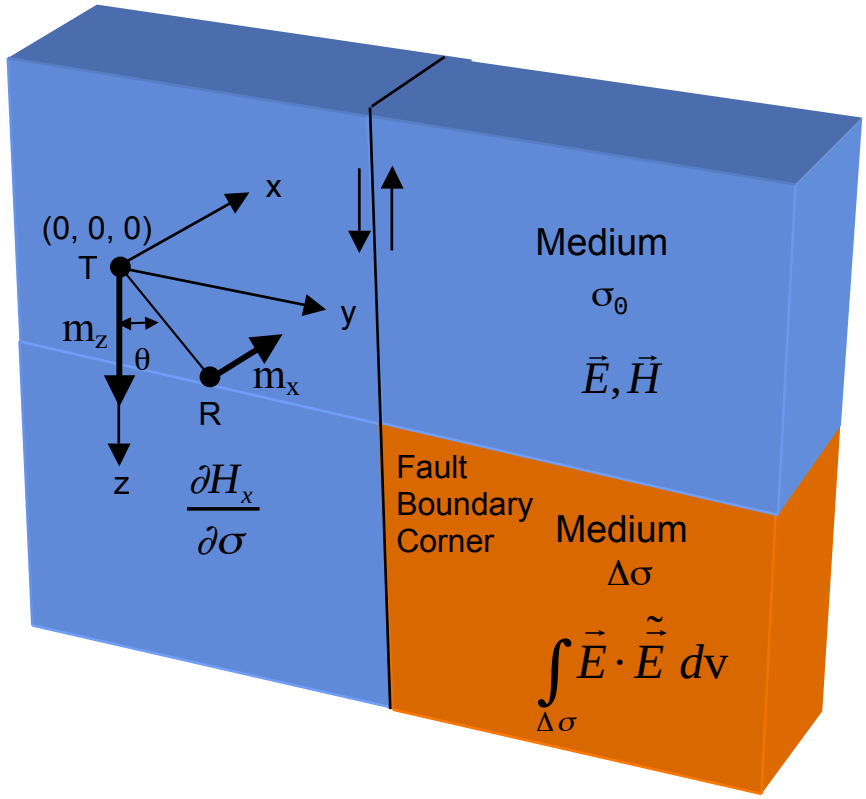

(a)

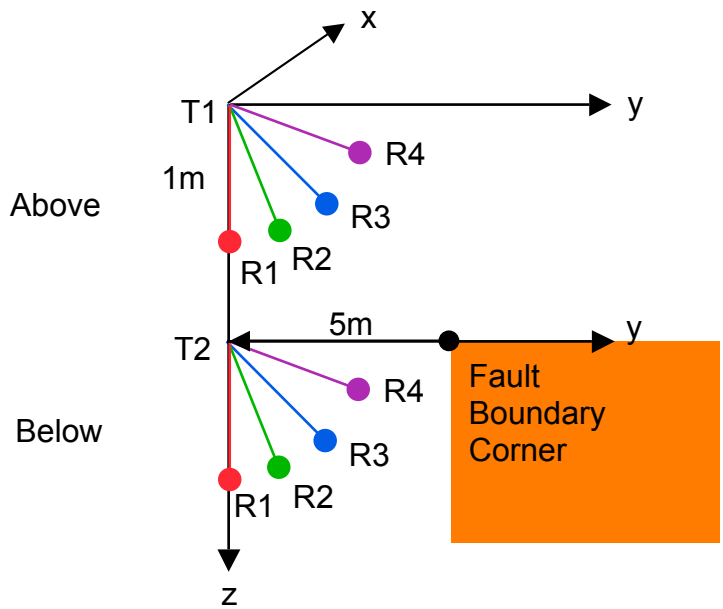

(b)

Figure 2: (a) The quarterspace fault model. (b) Sensitivities are calculated for tool locations above and below the fault boundary corner (FBC) in the *y*-*z* plane. Receivers are located at 0, 30, 45, and 60 degrees respectively from the vertical *z*-direction.

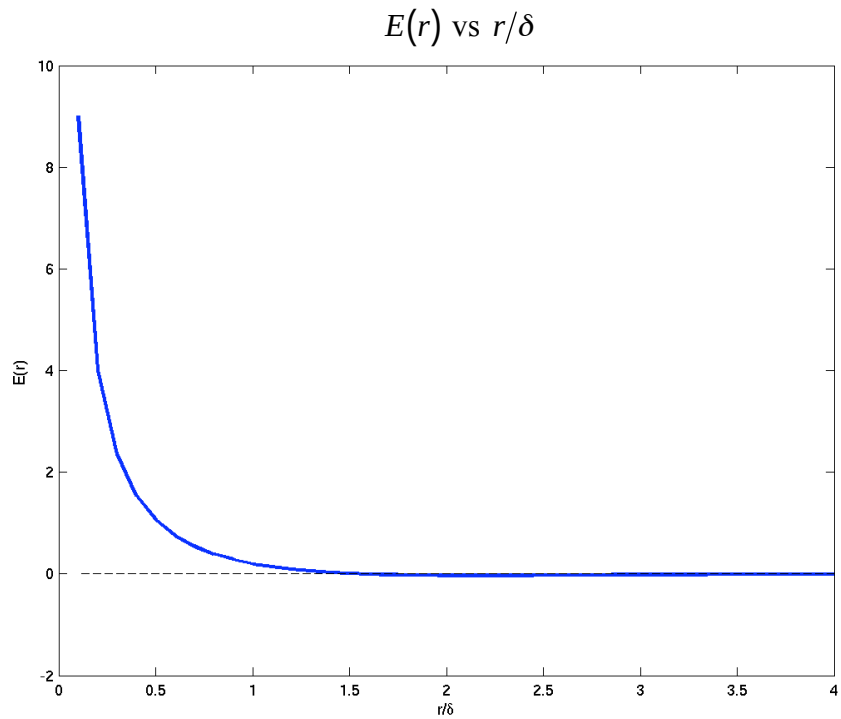

Figure 3: Illustration of the radial dependence of the magnitude of the electric field $E(r)$ Eq.(25), as a function of skin depth δ for $f = 20{,}000$ Hz and $\sigma = 0.25$ S/m.

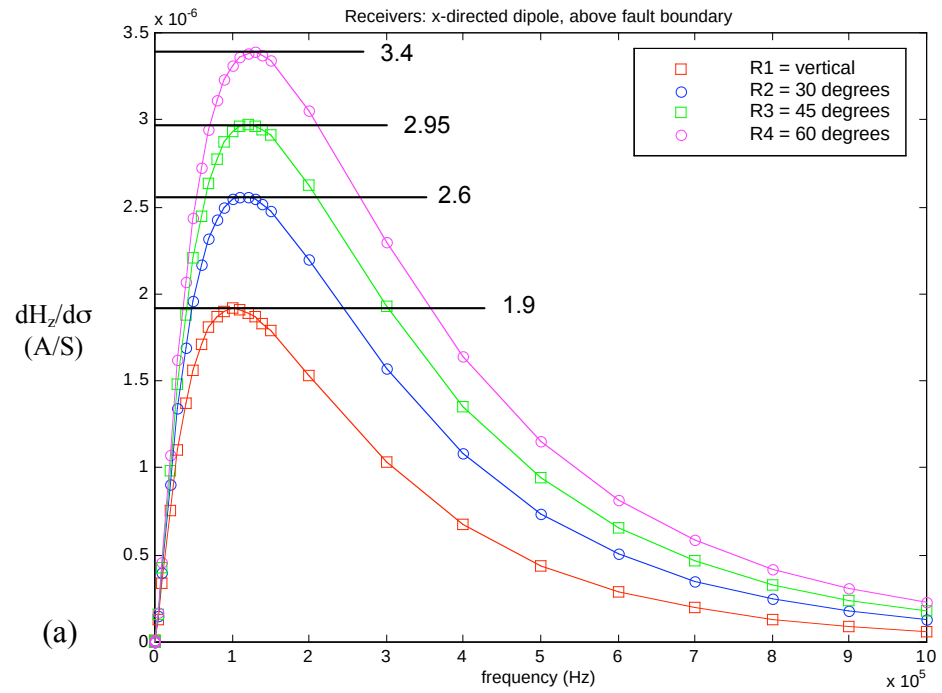

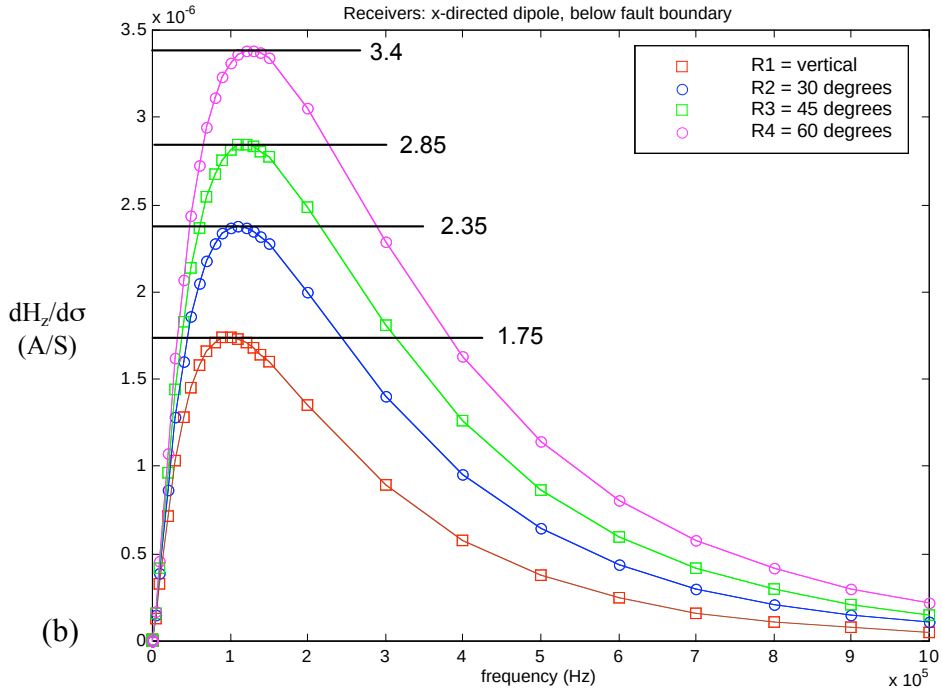

Figure 4: Sensitivities in the frequency domain in the *y*-*z* plane for a transmitter dipole in the *z*-direction and receiver dipoles in the *x*-direction (a) above and (b) below the fault boundary corner.

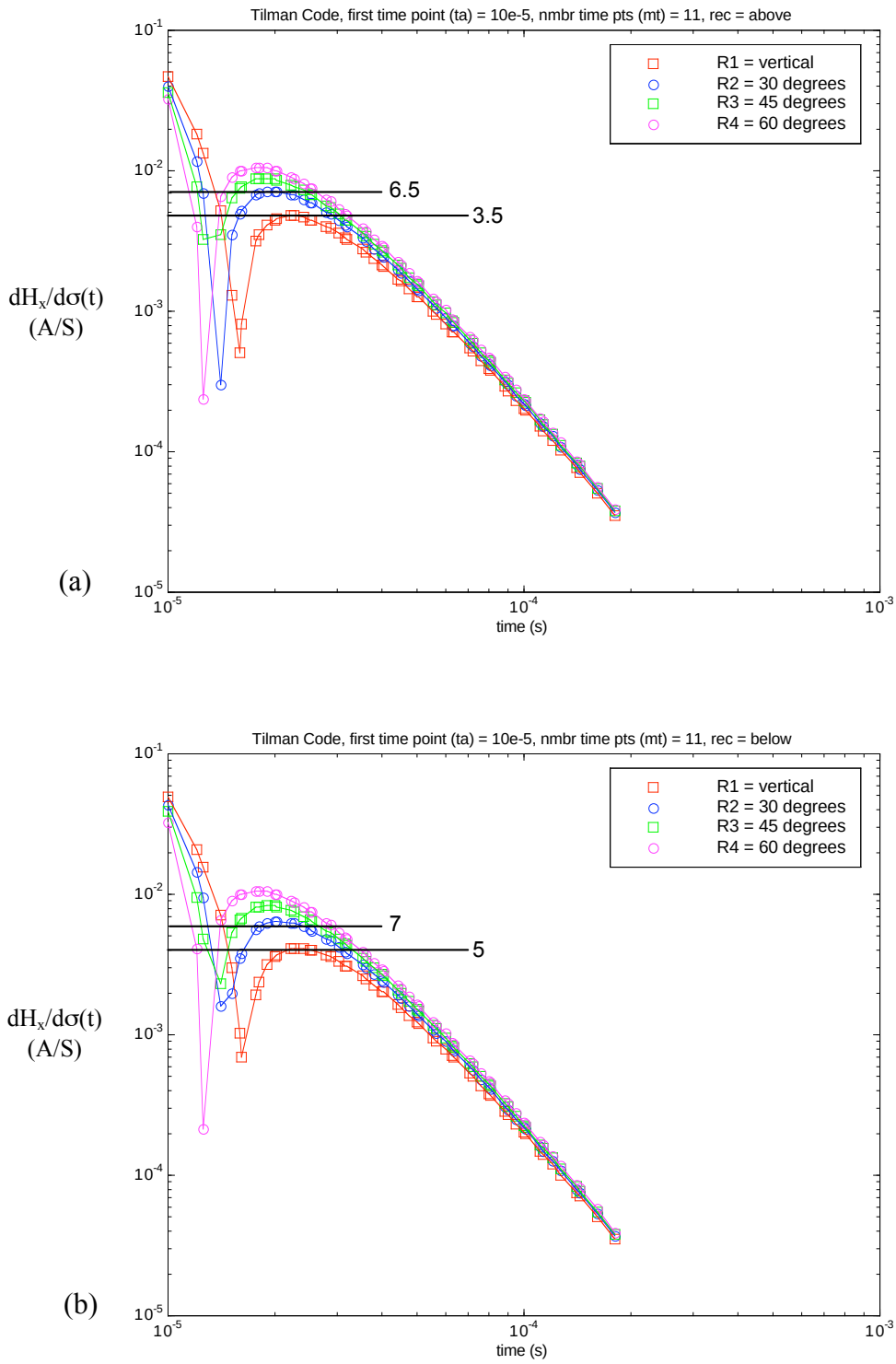

Figure 5: Time domain sensitivity plots in the *y*-*z* plane for a transmitter dipole in the *z*-direction and receiver dipoles in the *x*-direction (a) above and (b) below the fault boundary corner.

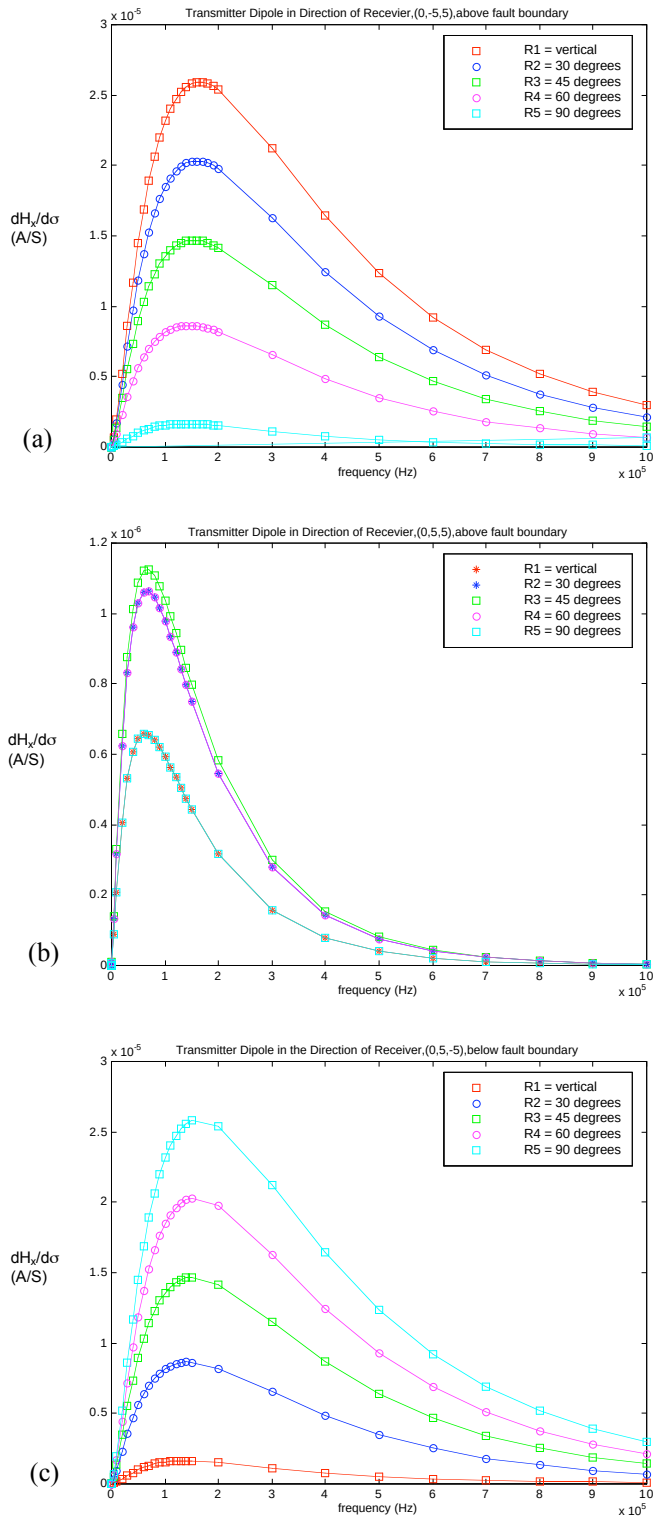

Figure 6: Sensitivities in the frequency domain in the *y-z* plane for the transmitter and the receivers (a) above (b) above and to the upper left and (c) below the fault block.

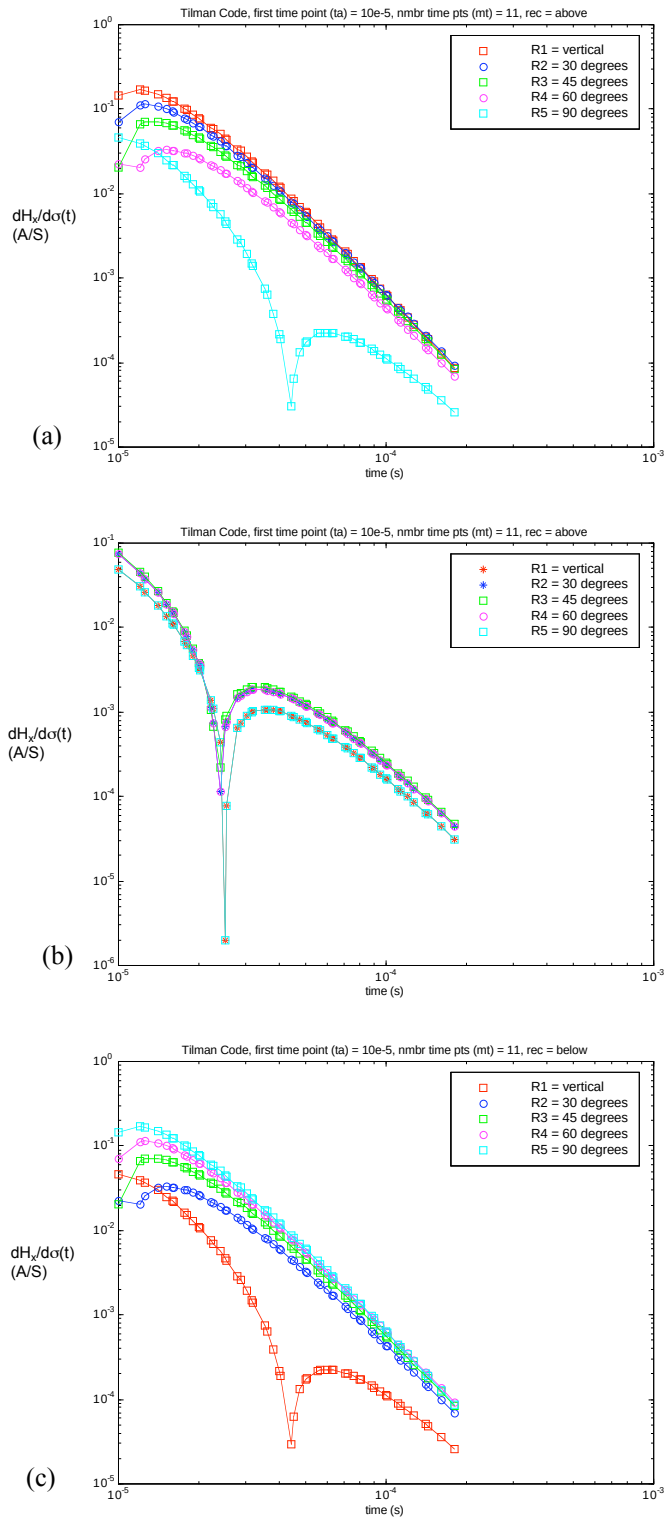

Figure 7: Sensitivities in the time domain in the *y*-*z* plane for the transmitter and the receivers (a) above (b) above and to the upper left and (c) below the fault block.

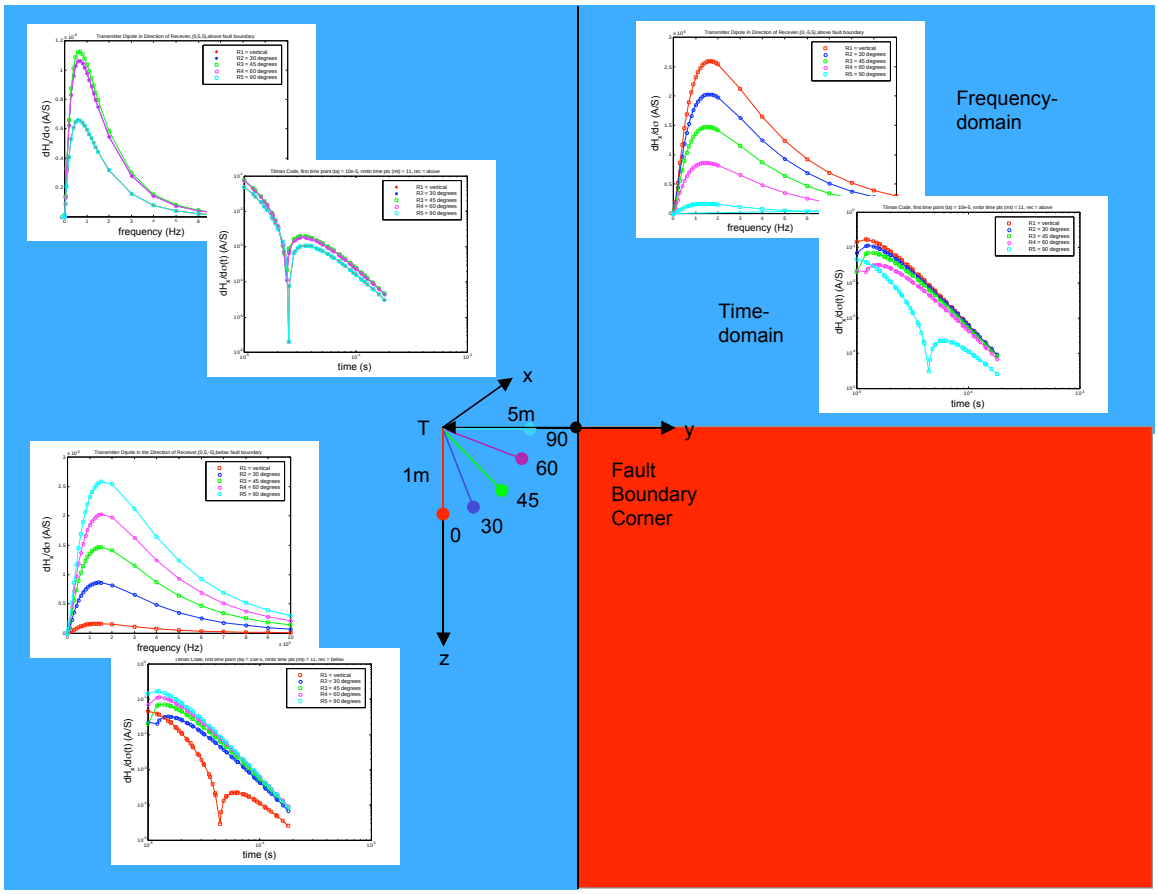

Figure 8: Sensitivities in the frequency and time domain in the *y-z* plane relative to the fault boundary corner.

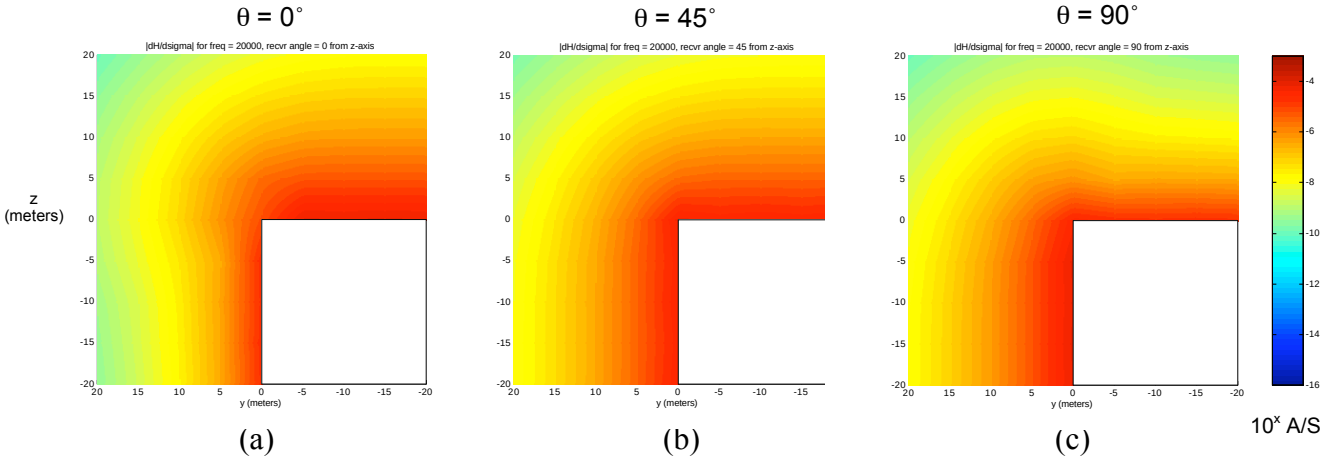

Figure 9: Symmetry of response shown for the various tool locations in the frequency domain. Sensitivities in the *y-z* plane were calculated around the fault boundary corner from zero to 20 meters, in five-meter intervals. For (a) the vertical sonde ($\theta = 0^\circ$), (b) for the sonde dipping at 45°($\theta = 45^\circ$) and (c) the horizontal sonde ($\theta = 90^\circ$).

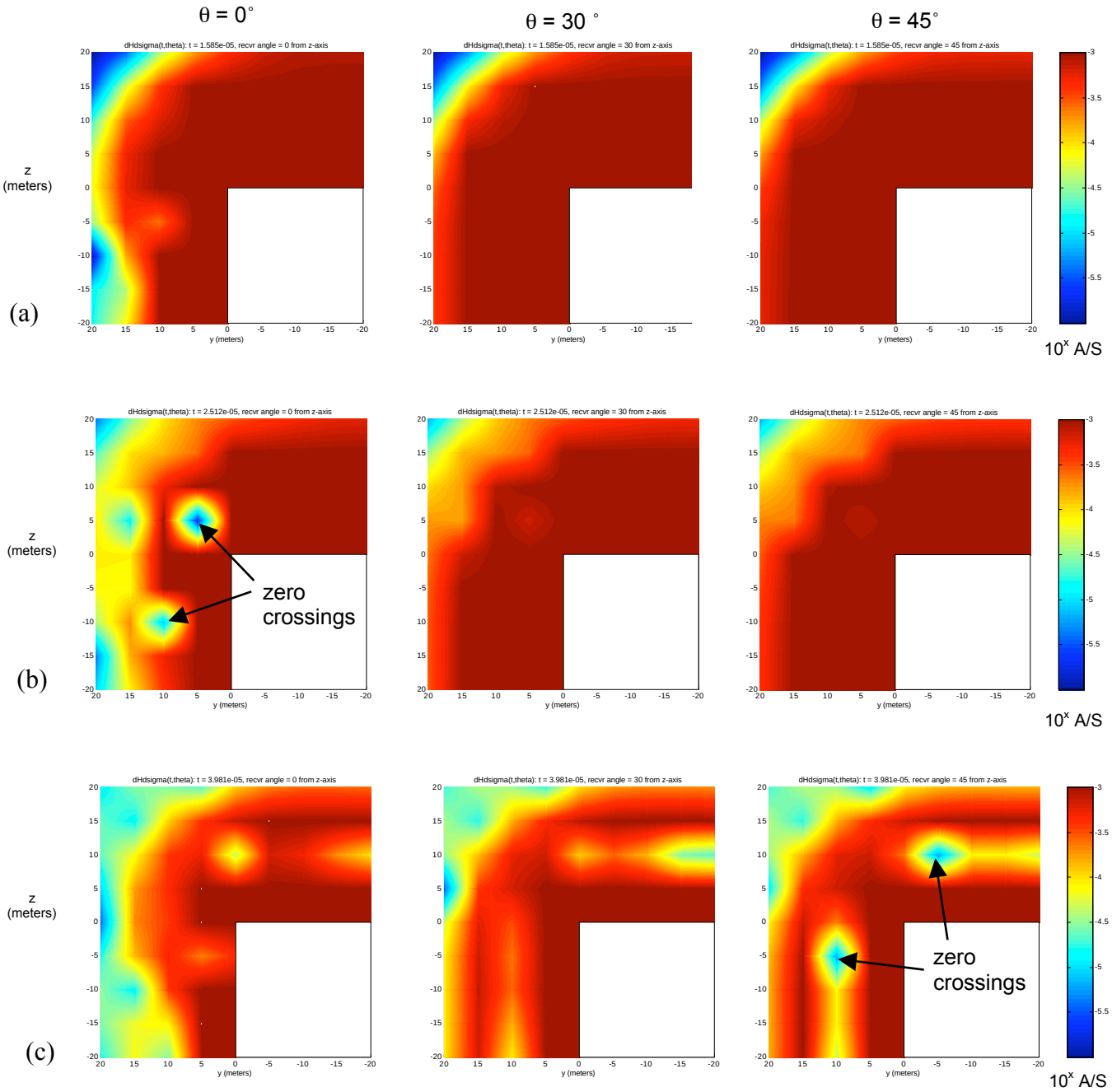

Figure 10: The symmetry of response shown in the time domain. Tool locations at 0°, 30° and 45° are shown for a fixed time (a) t = 1.5 x$10^{-5;}$ (b) For t = 2.5 x 10^{-5}, the cusps (or zero crossings) can clearly be seen for the vertical sonde; and (c) at t = 3.9 x 10^{-5}, the cusps (or zero crossings) can also be seen for all tool locations.

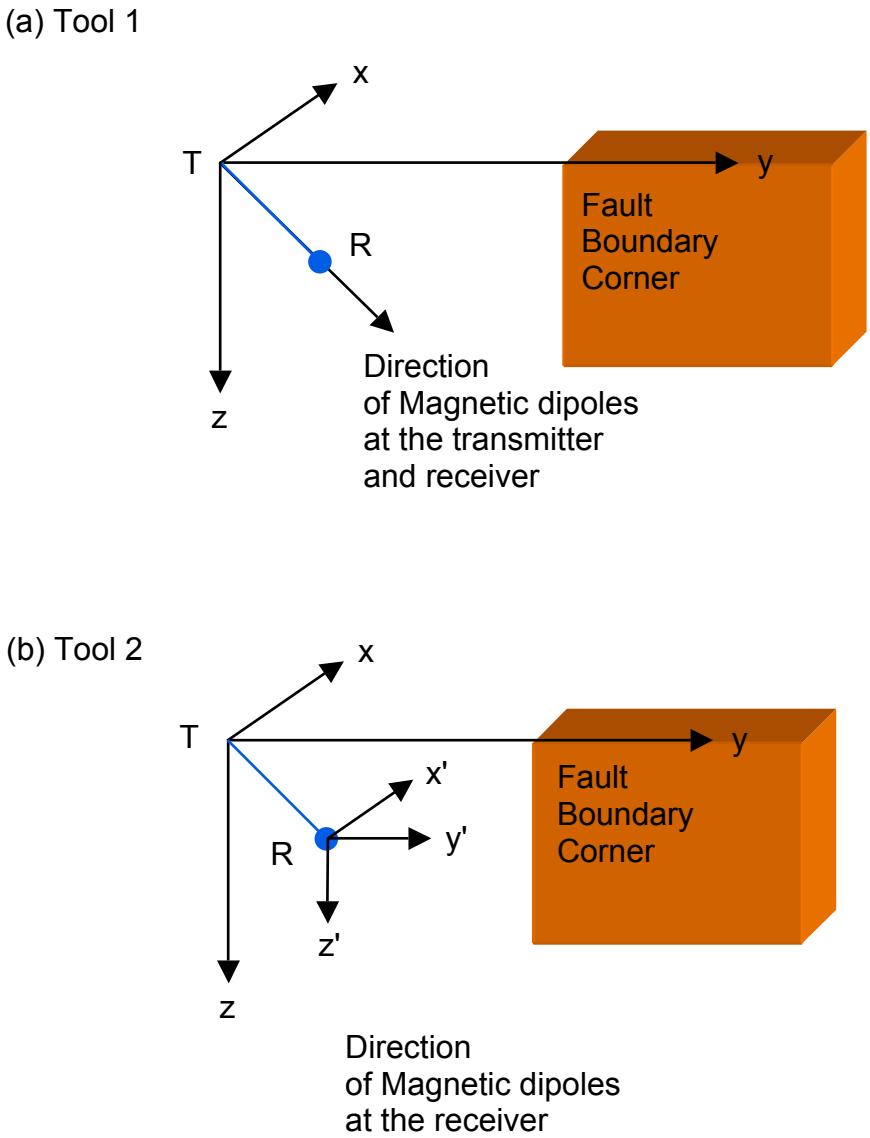

Figure 11: Tool locations around the fault boundary corner. Sensitivities in the frequency domain were calculated for (a) tool 1, transmitter and receiver dipoles in the direction of the tool orientation and (b) tool 2, transmitter dipole in the direction of the receiver and an *x,y, or z*-directed magnetic dipole at the receiver. In the case the *x,y,z* coordinates of the receiver dipoles follow the absolute *x,y,z* coordinates of the fault corner boundary.

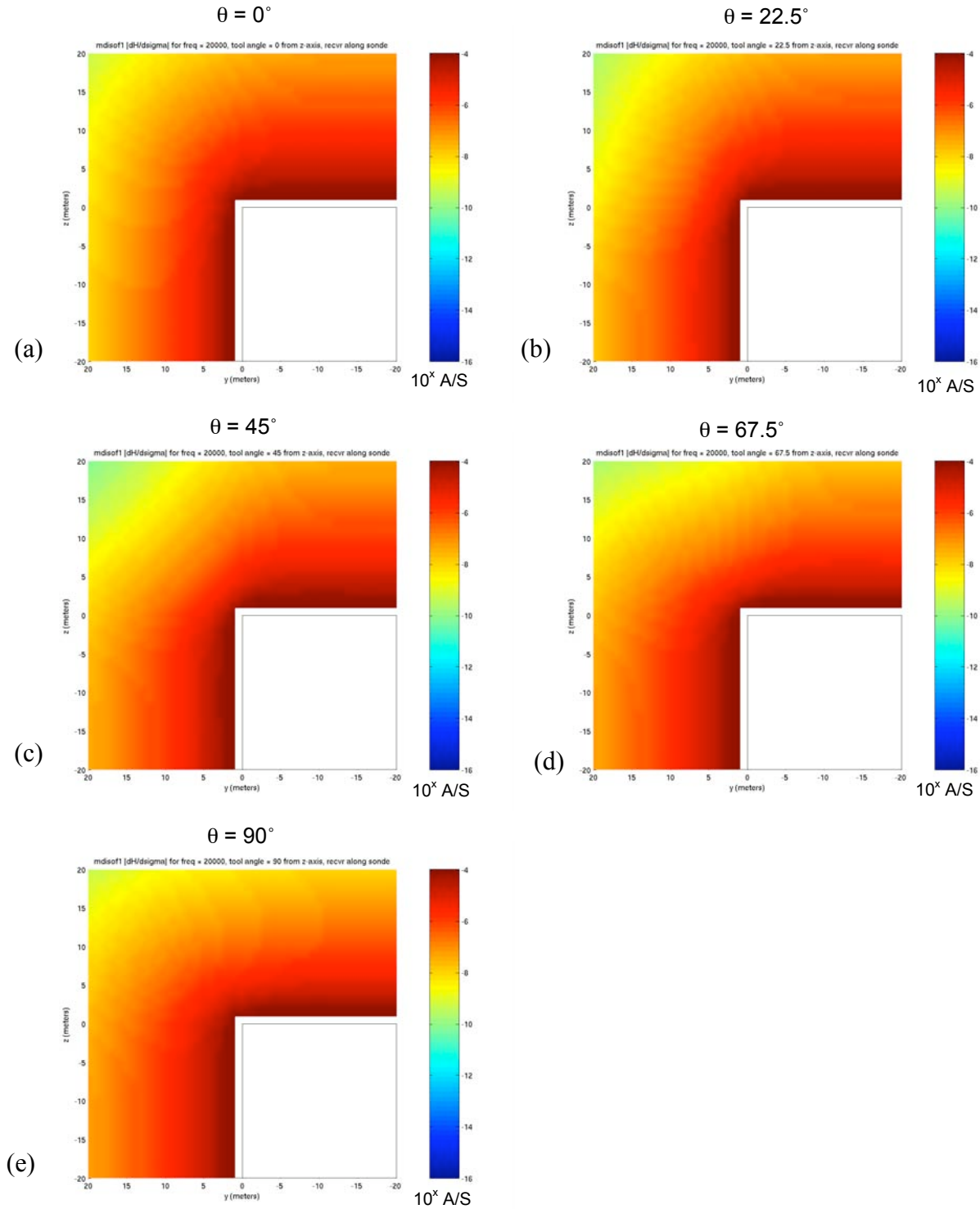

Figure 12: Higher resolution runs in the frequency domain for tool 1, transmitter and receiver dipole in the direction of the tool orientation. Sensitivities in the *y-z* plane were calculated around the fault boundary corner from zero to 20 meters, in one-meter intervals. Frequency = 20,000 Hz, wholespace conductivity = 0.25 S/m, for (a) the vertical sonde (θ= 0˚), (b) the sonde dipping at 22.5˚(θ= 22.5˚), (c) 45˚(θ= 45˚), (d) 67.5˚(θ= 67.5˚), and (e) the horizontal sonde (θ = 90˚).

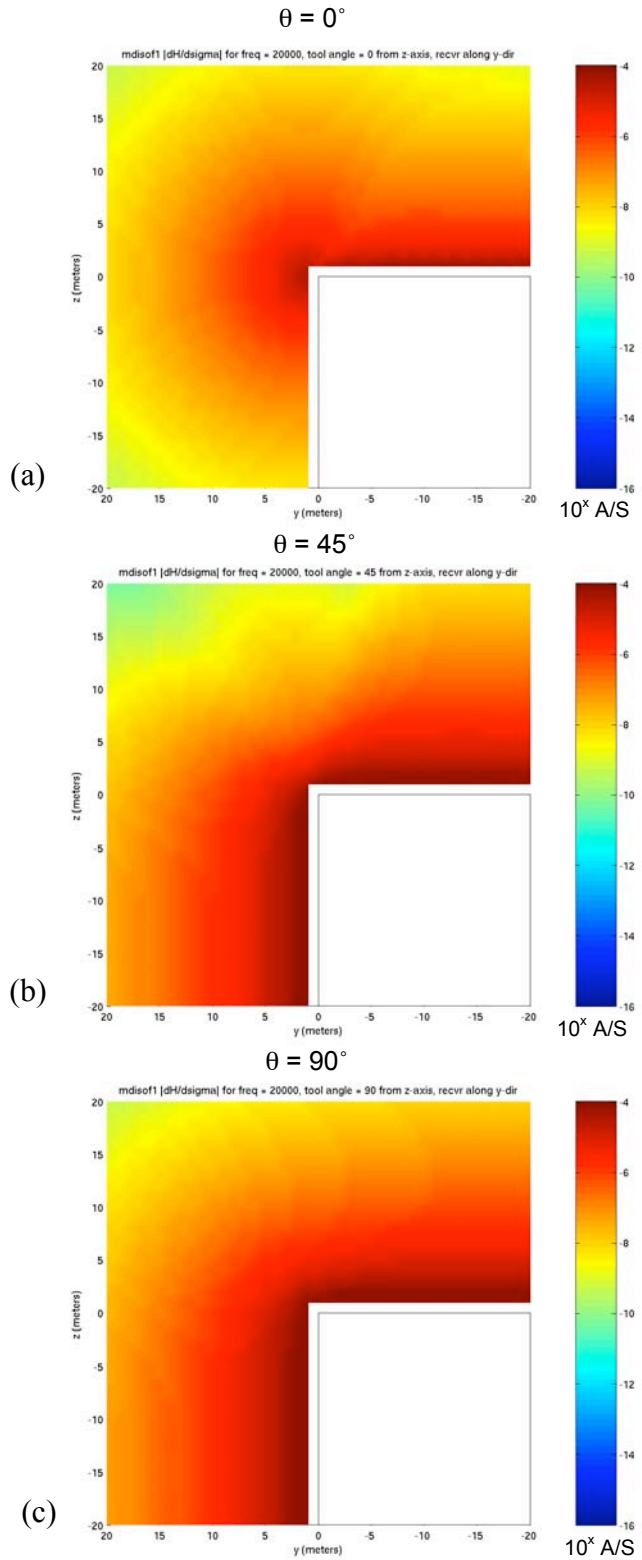

Figure 13: Higher resolution runs in the frequency domain for tool 2, transmitter dipole in the direction of the tool orientation and receiver dipole in the *y*-direction. Frequency = 20,000 Hz, wholespace conductivity = 0.25 S/m, for (a) the vertical sonde (θ= 0˚), (b) the sonde dipping at 45˚(θ= 45˚), and (b) the horizontal sonde (θ = 90˚).

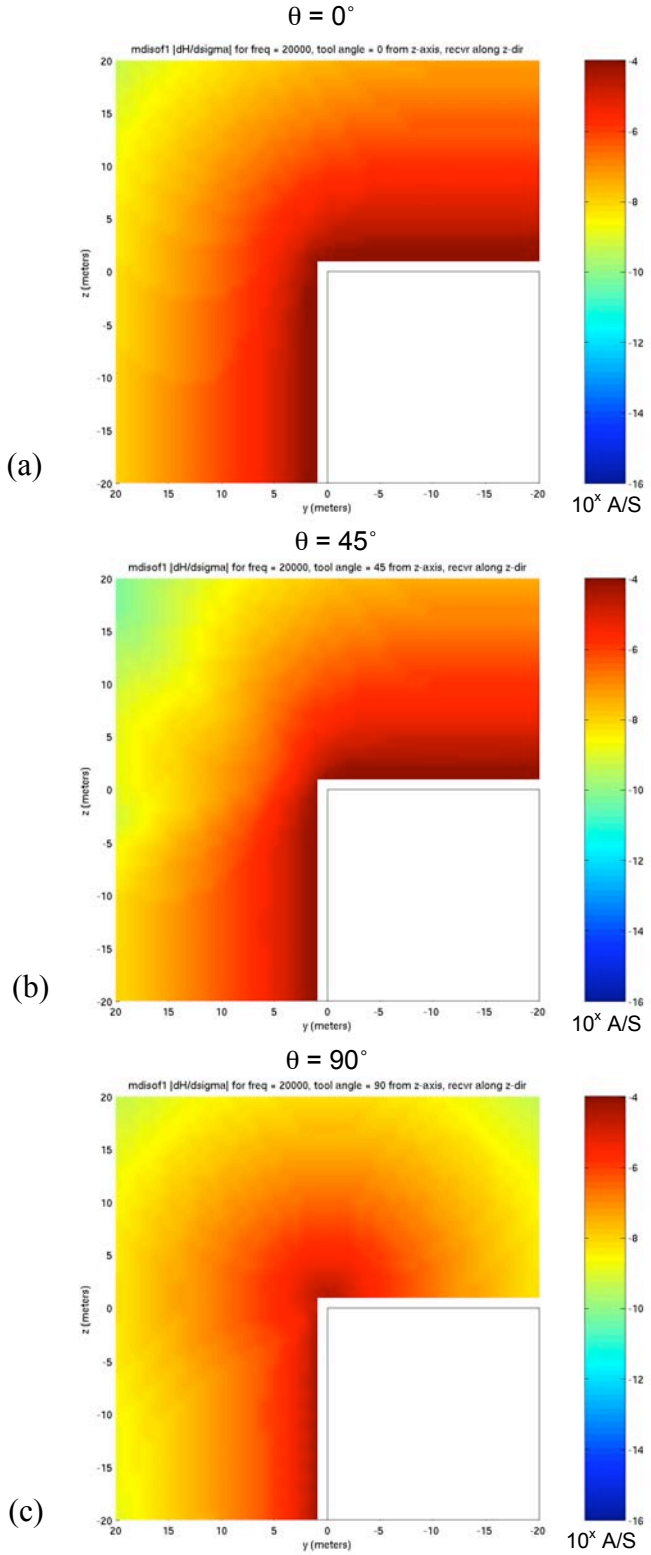

Figure 14: Higher resolution runs in the frequency domain for tool 2, transmitter dipole in the direction of the tool orientation and receiver dipole in the *z*-direction. Frequency = 20,000 Hz, wholespace conductivity = 0.25 S/m, for (a) the vertical sonde (θ= 0˚), (b) the sonde dipping at 45˚(θ= 45˚), and (b) the horizontal sonde (θ = 90˚).

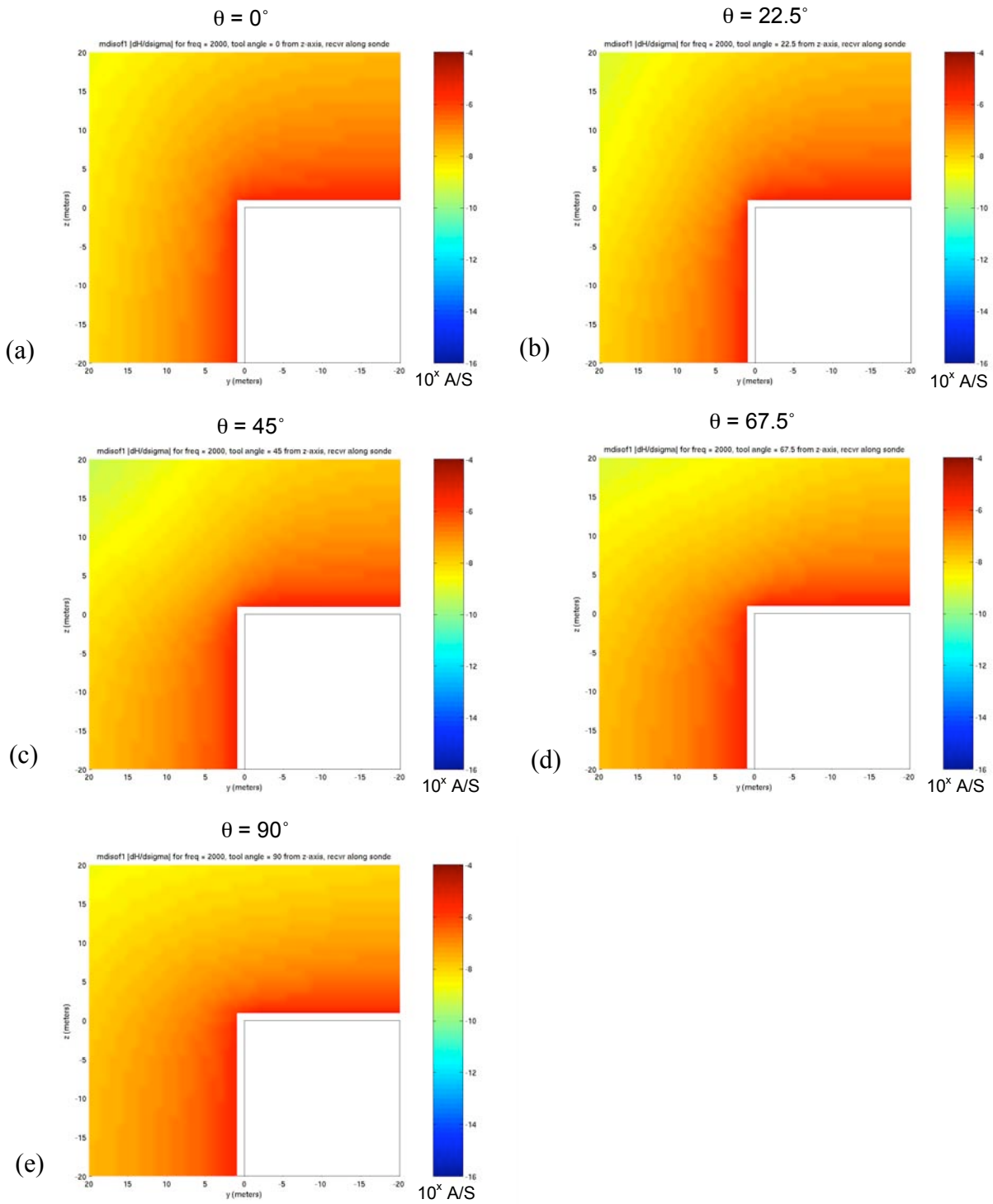

Figure 15: Higher resolution runs in the frequency domain for tool 1, transmitter and receiver dipole in the direction of the tool orientation. Frequency = 2000 Hz, wholespace conductivity = 0.25 S/m, for (a) the vertical sonde (θ= 0˚), (b) the sonde dipping at 22.5˚(θ= 22.5˚), (c) 45˚(θ= 45˚), (d) 67.5˚(θ= 67.5˚), and (e) the horizontal sonde (θ = 90˚).

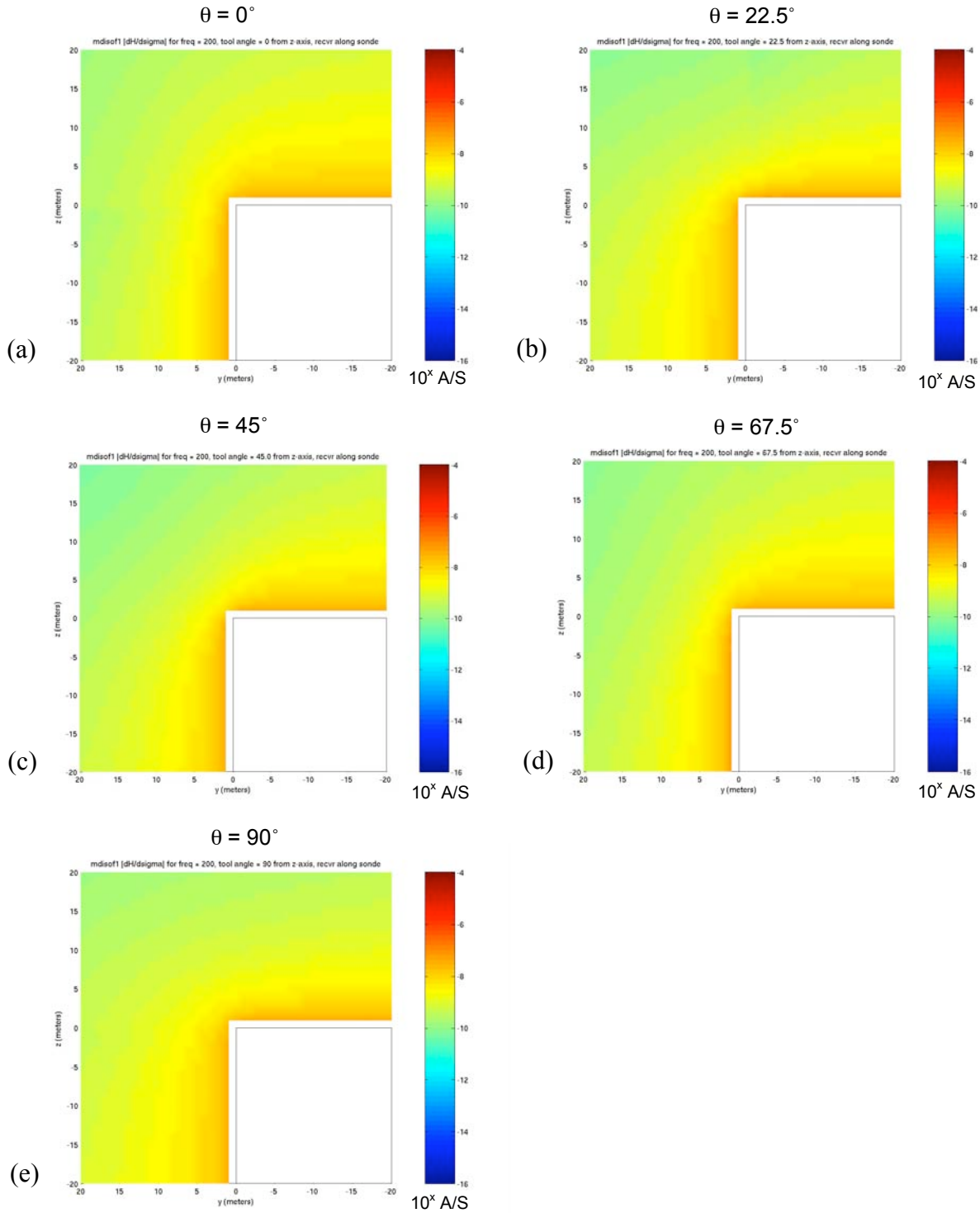

Figure 16: Higher resolution runs in the frequency domain for tool 1, transmitter and receiver dipole in the direction of the tool orientation. Frequency = 200 Hz, wholespace conductivity = 0.25 S/m, for (a) the vertical sonde (θ= 0˚), (b) the sonde dipping at 22.5˚(θ= 22.5˚), (c) 45˚(θ= 45˚), (d) 67.5˚(θ= 67.5˚), and (e) the horizontal sonde (θ = 90˚).

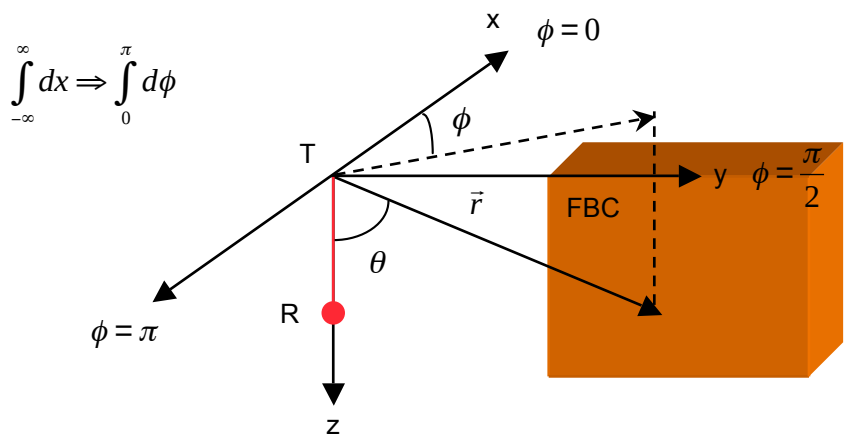

Figure 17. The integration over x is equivalent to an integration over the azimuthal angle ϕ from 0 to π.

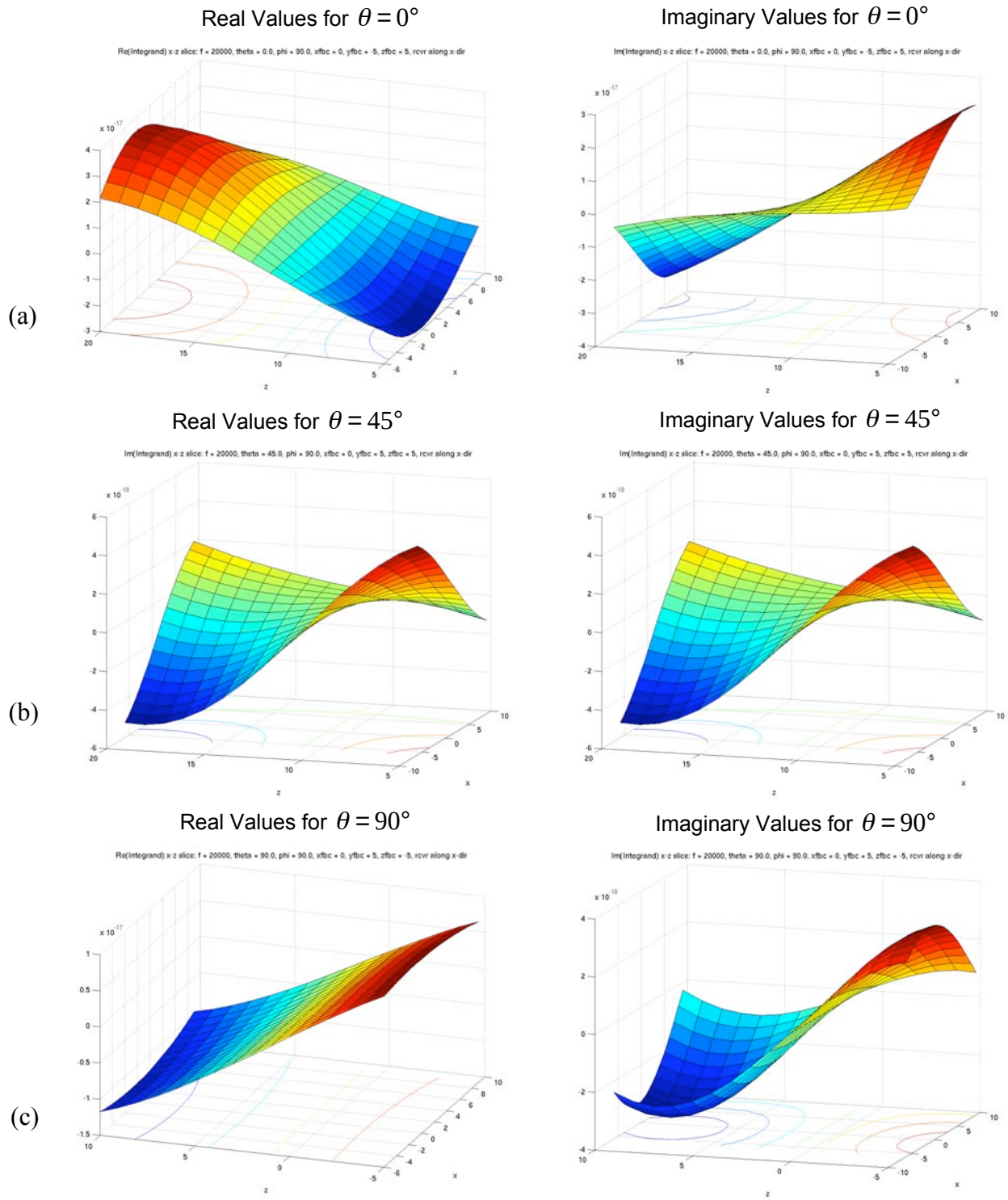

Figure 18: The integrand in the frequency domain for tool 2, transmitter dipole in the direction of the tool orientation and receiver dipole in the x-direction. Frequency = 20,000 Hz, wholespace conductivity = 0.25 S/m, for the real and imaginary values for (a) the vertical sonde ($\theta = 0°$), (b) the sonde dipping at 45° ($\theta = 45°$), and (c) the horizontal sonde ($\theta = 90°$), in the y-z plane 5 meters away form the fault boundary corner.

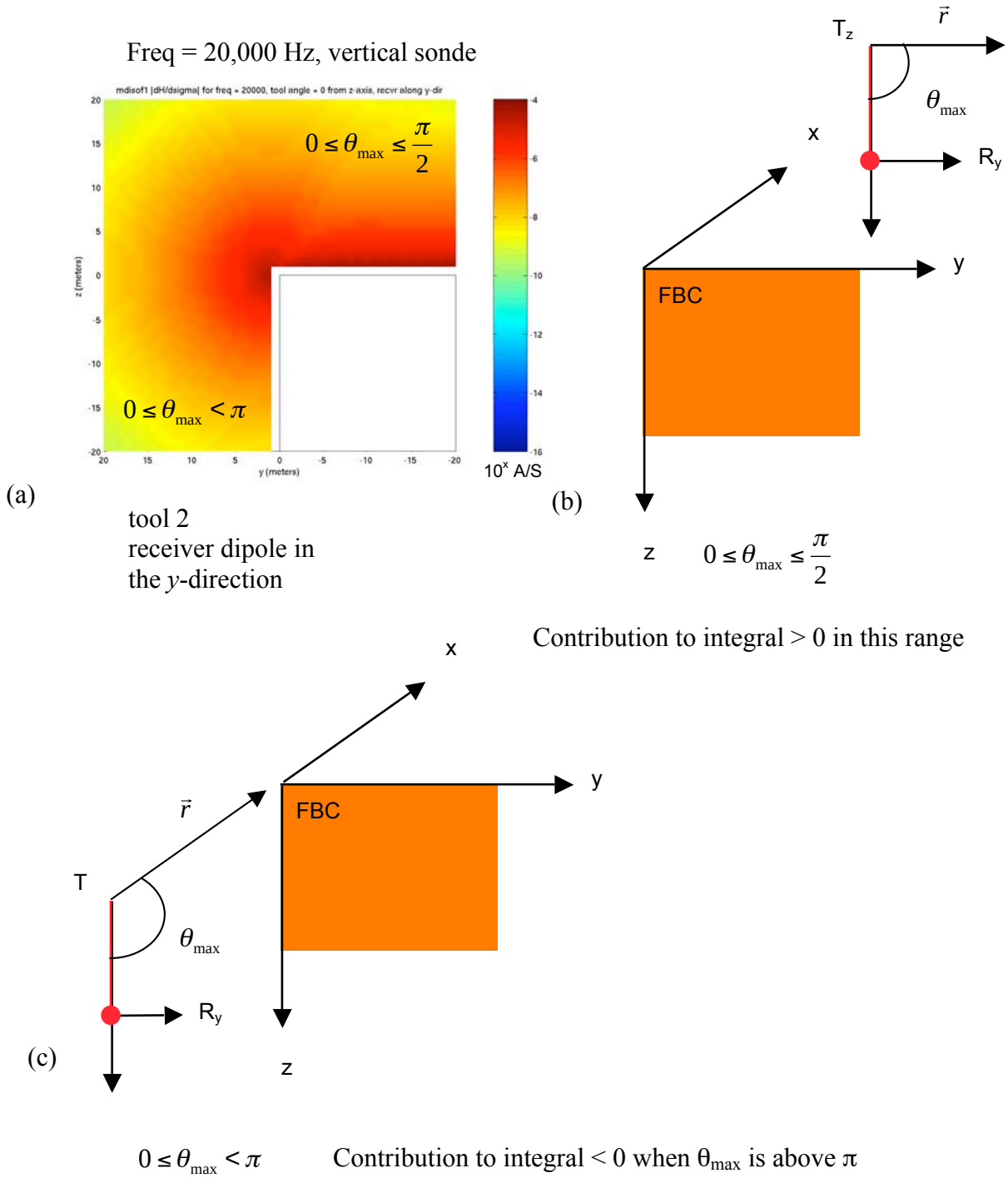

Figure 19. The "Keyhole" feature. For the case when transmitter and receiver dipoles are 90° apart, this feature can be explained by the relative position (above/below) of the transmitter to the fault boundary corner.

Receiver dipole in the *z*-direction

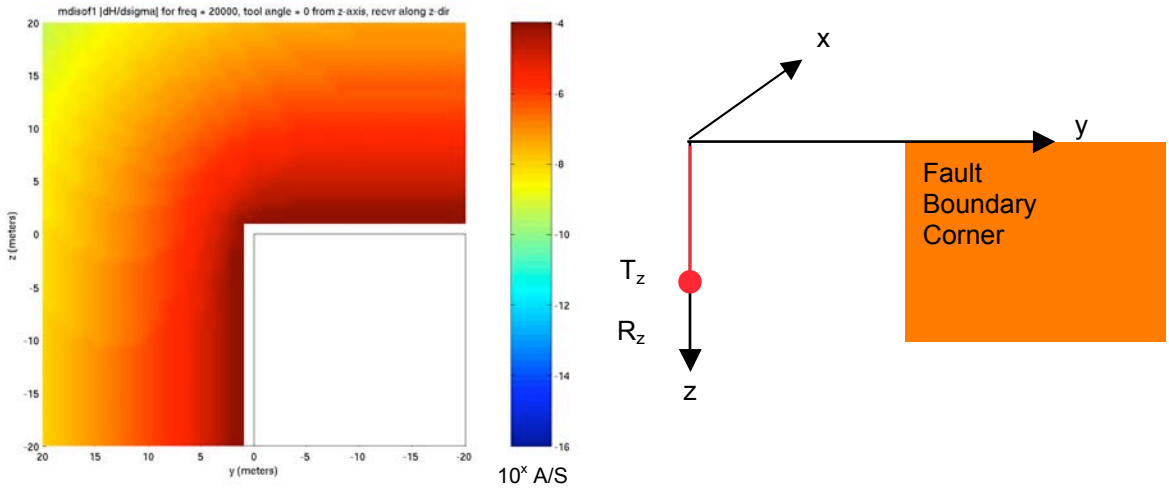

(a)

Receiver dipole in the *y*-direction

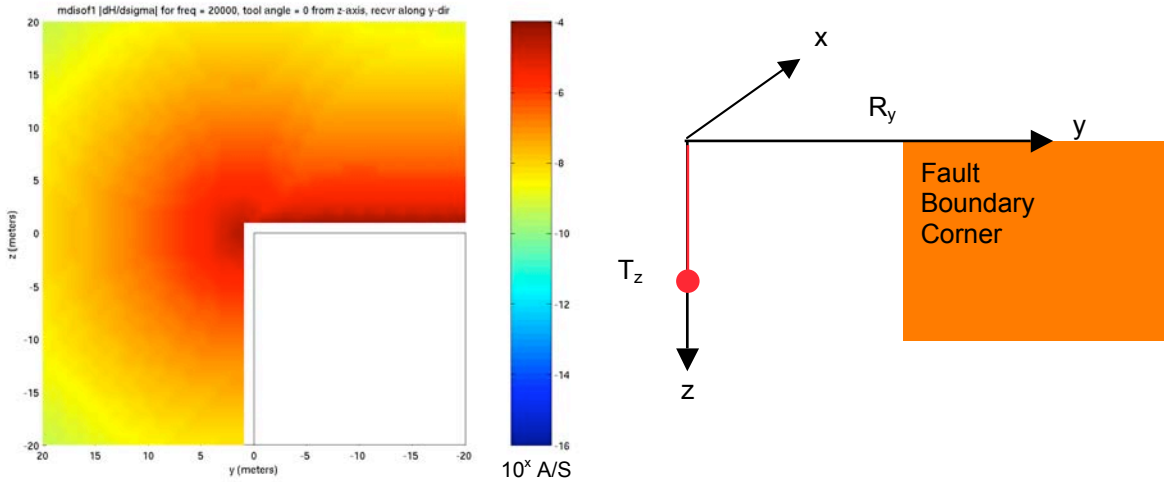

(b)

Figure 20. Strongest vs. weakest magnitudes of the sensitivities. (a) The strongest magnitude of the sensitivities occurs when the transmitter and receiver dipoles are in the same direction. (b) The weakest magnitudes occur when the transmitter and receiver dipoles are 90˚ apart.

(a)

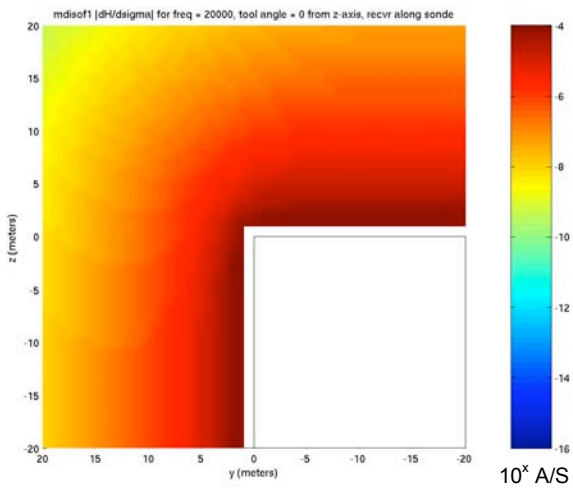

Freq = 20,000 Hz

$$\vec{E}_T \cdot \tilde{\vec{E}}_R \sim \omega^2$$

(b)

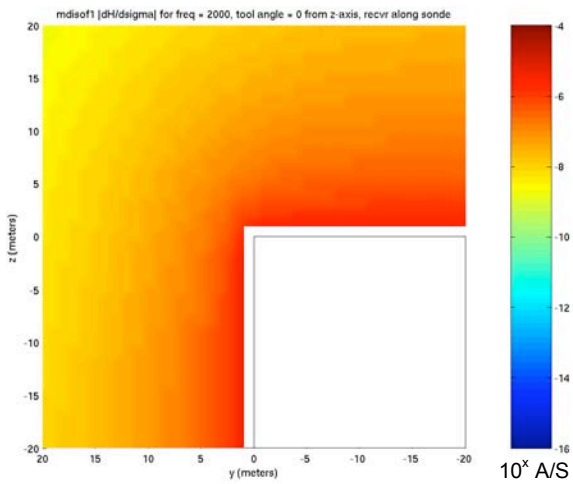

Freq = 2000 Hz

$$\vec{E}_T \cdot \tilde{\vec{E}}_R \sim \left(\frac{\omega}{10}\right)^2 = \frac{\omega^2}{10^2}$$

(c)

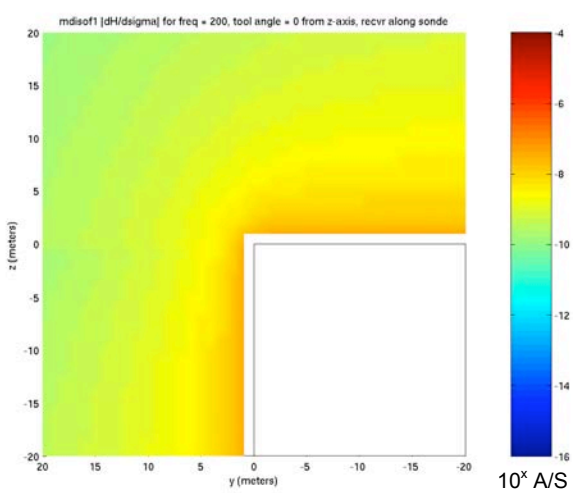

Freq = 200 Hz

$$\vec{E}_T \cdot \tilde{\vec{E}}_R \sim \left(\frac{\omega}{100}\right)^2 = \frac{\omega^2}{10^4}$$

Figure 21: Overall magnitude of the sensitivities can be addressed as the frequency is varied. The strongest magnitude sensitivities occur for (a) the larger frequencies.

(a)

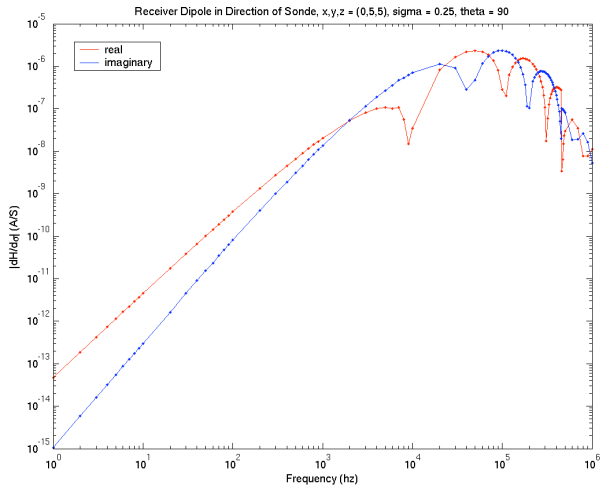

(b)

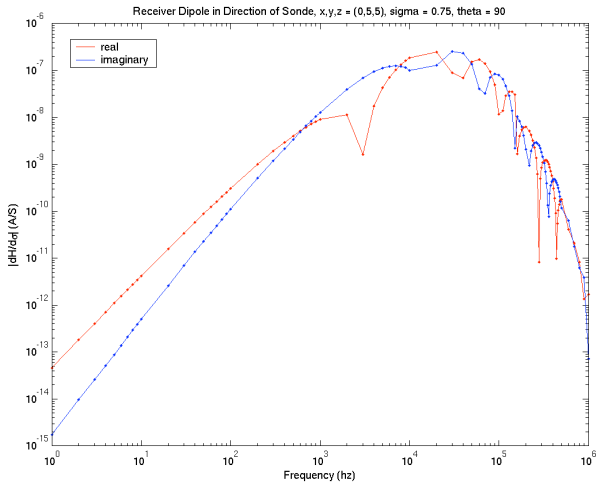

(c)

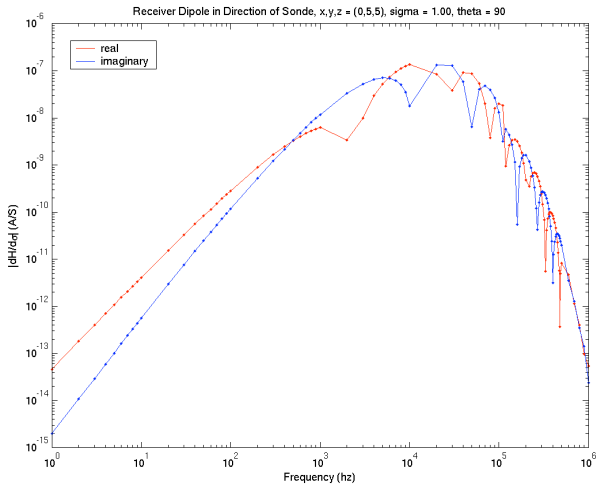

Figure 22: Real and imaginary sensitivity values in the frequency domain in the *y-z* plane for the receiver dipole in the direction of the sonde, receiver angle = 90˚, *x,y,z* = (0,5,5) above the fault boundary corner with conductivity (a) 0.25, (b) 0.75 and (c) 1.0 S/m.

(a)

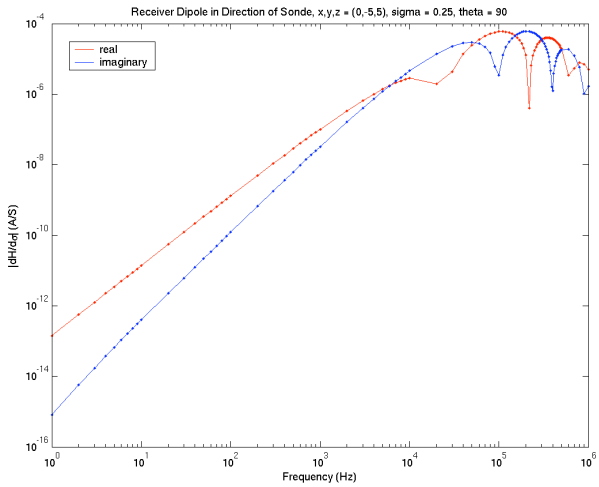

(b)

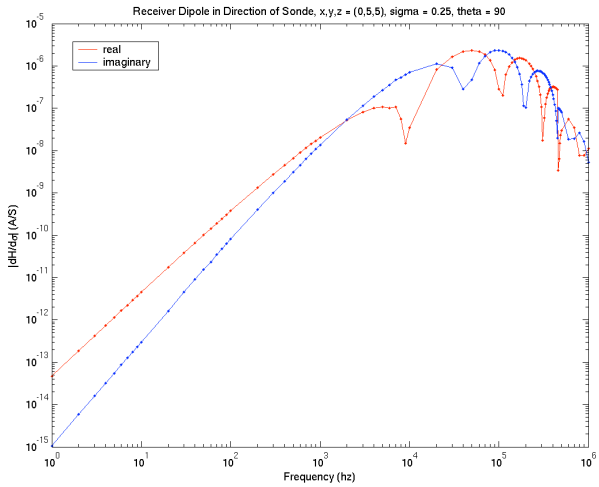

(c)

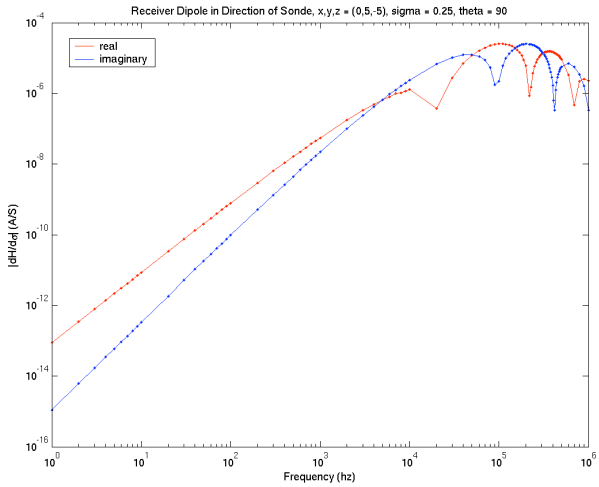

Figure 23: Real and imaginary sensitivity values in the frequency domain in the *y-z* plane for the transmitter and receiver dipole in the direction of the sonde, receiver angle = 90˚, with conductivity 0.25 for (a) above, (b) above and to the left and (c) below at a five meter distance from the fault boundary corner.

(a)

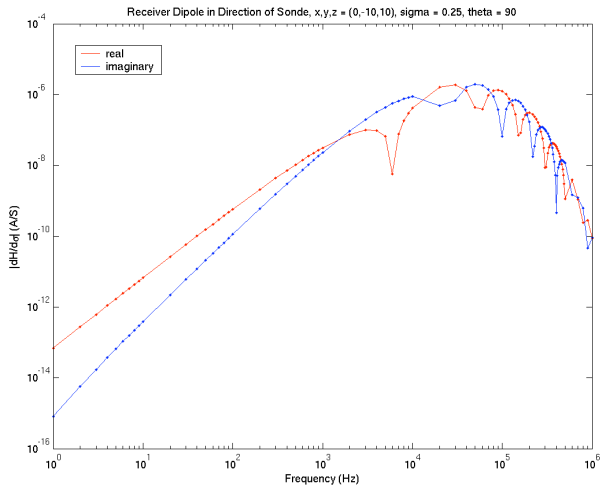

(b)

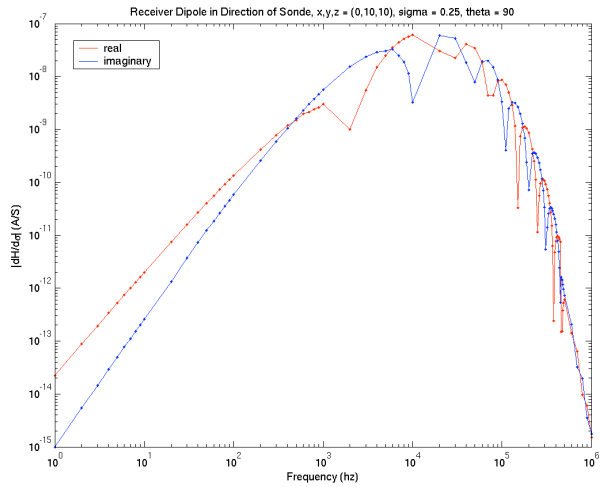

(c)

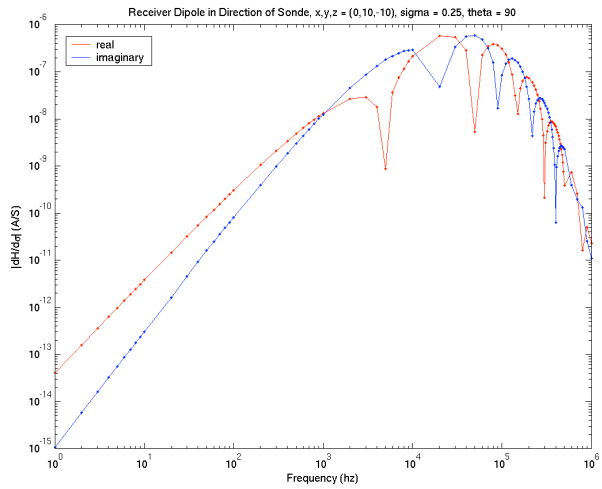

Figure 24: Real and imaginary sensitivity values in the frequency domain in the *y-z* plane for the transmitter and receiver dipole in the direction of the sonde, receiver angle = 90˚, with conductivity 0.25 for (a) above, (b) above and to the left and (c) below at a ten meter distance from the fault boundary corner.

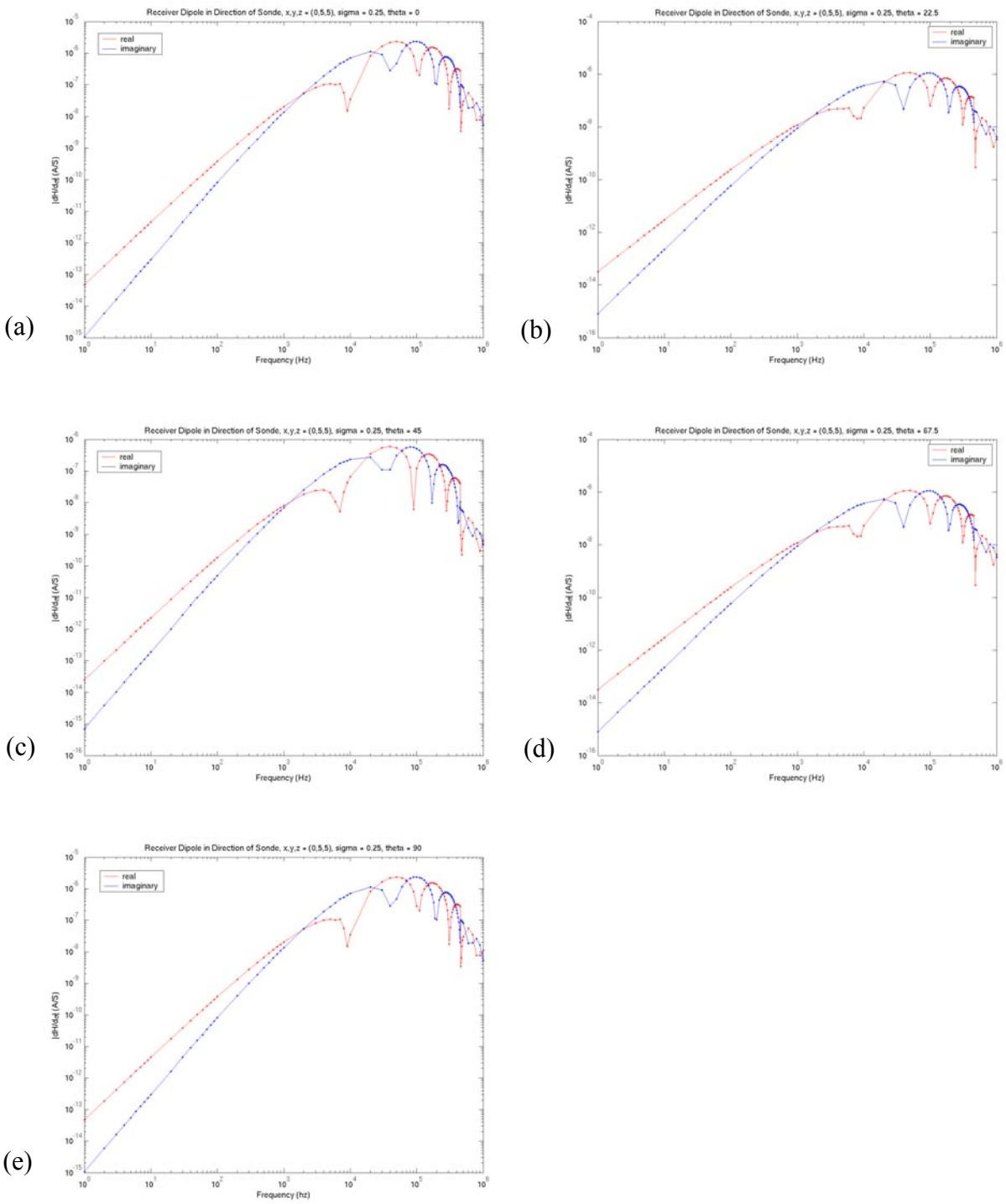

Figure 25: Real and imaginary sensitivity values in the frequency domain in the *y-z* plane for the transmitter and receiver dipole in the direction of the sonde with conductivity 0.25 for (a) the vertical sonde (θ= 0˚), (b) the sonde dipping at 22.5˚(θ= 22.5˚), (c) 45˚(θ= 45˚), (d) 67.5˚(θ= 67.5˚), and (e) the horizontal sonde (θ = 90˚) above the fault block.

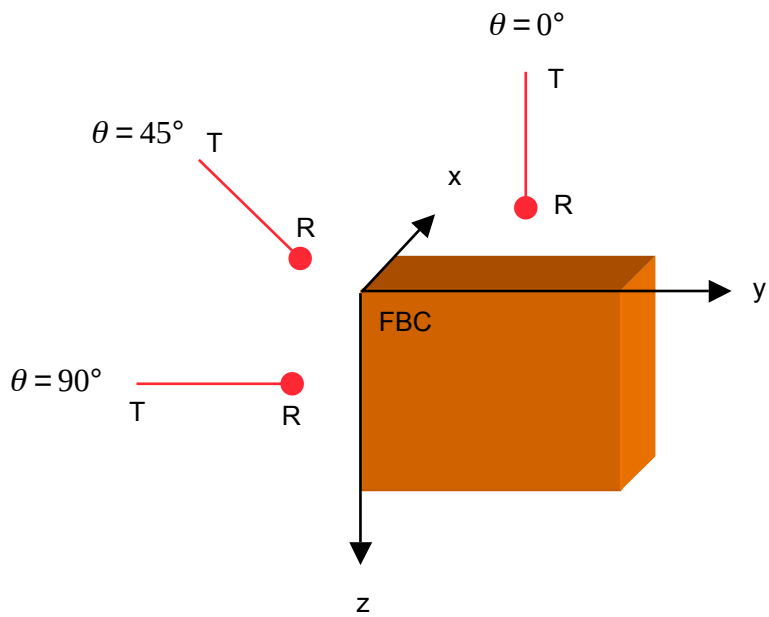

Figure 26: The integrand $\vec{E}_T(\vec{x}) \cdot \tilde{\vec{E}}_R(\vec{x})$ of Eq.(13) was plotted for the frequency domain for tool 1, transmitter dipole and receiver dipole in the direction of the tool orientation. Frequencies 20,000 Hz, 200Hz and 200 Hz, wholespace conductivity = 0.25 S/m, for the vertical sonde above, the sonde dipping at 45˚ above and to the right, and the horizontal sonde below the fault boundary corner.

(a)

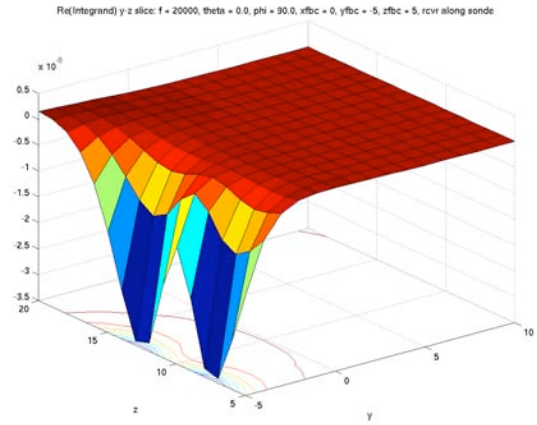

(b)

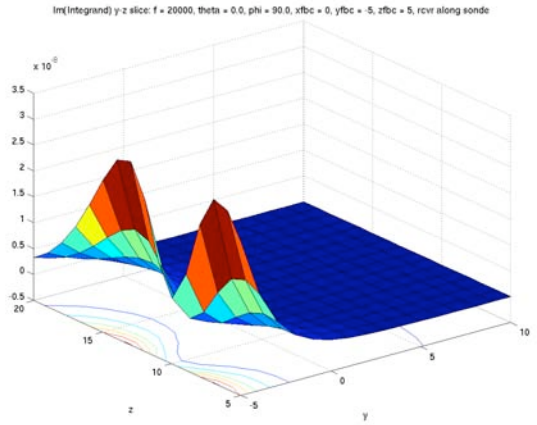

(c)

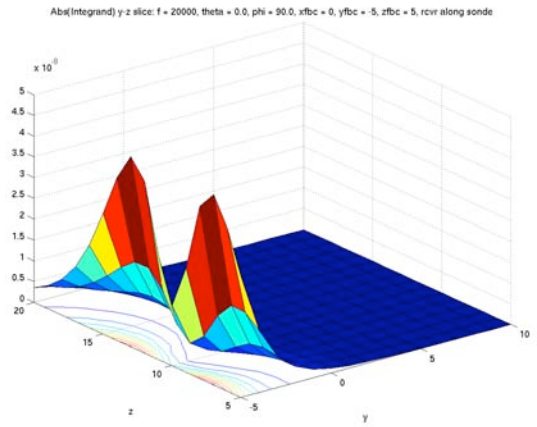

Figure 27: The integrand in the frequency domain for tool 1, transmitter dipole and receiver dipole in the direction of the tool orientation. Frequency = 20,000 Hz, wholespace conductivity = 0.25 S/m, for the vertical sonde in the *y-z* plane 5 meters away form the FBC, showing (a) the real, (b) the imaginary and (c) the absolute values.

(a)

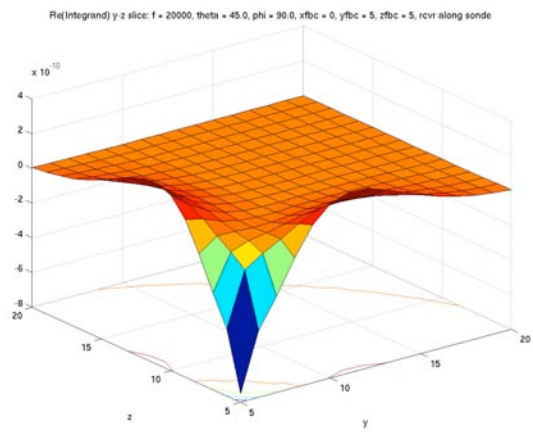

(b)

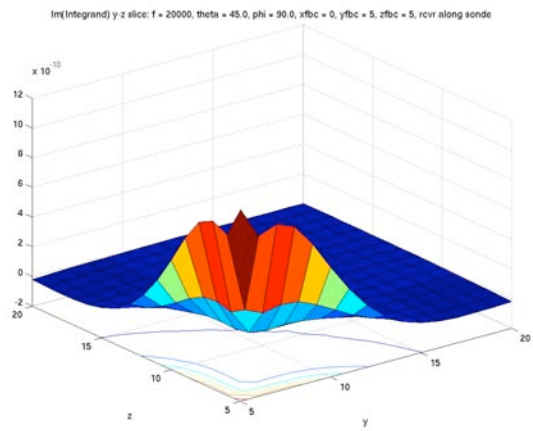

(c)

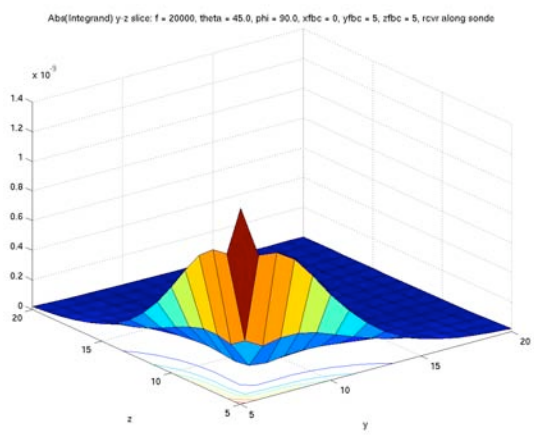

Figure 28: The integrand in the frequency domain for tool 1, transmitter dipole and receiver dipole in the direction of the tool orientation. Frequency = 20,000 Hz, wholespace conductivity = 0.25 S/m, for the sonde dipping 45˚ in the *y-z* plane 5 meters to the above right of the FBC, showing (a) the real values, (b) the imaginary values, and (c) the absolute values.

(a)

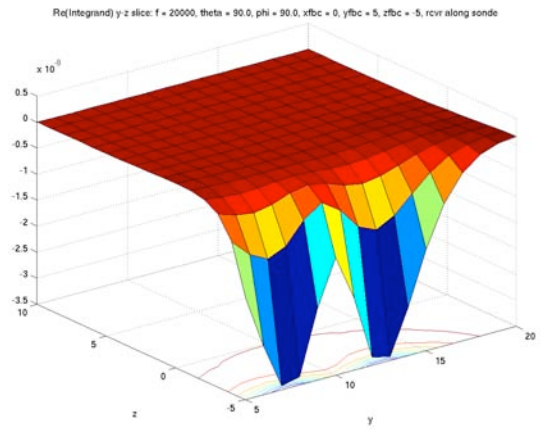

(b)

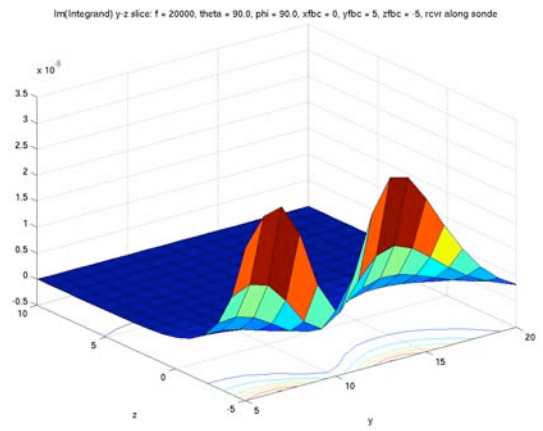

(c)

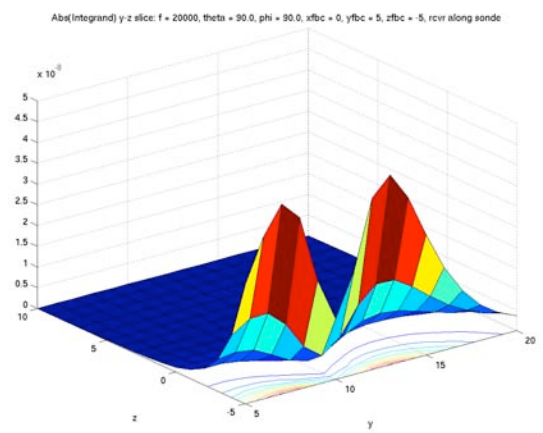

Figure 29: The integrand in the frequency domain for tool 1, transmitter dipole and receiver dipole in the direction of the tool orientation. Frequency = 20,000 Hz, wholespace conductivity = 0.25 S/m, for the horizontal sonde in the *y*-*z* plane 5 meters below the fault boundary corner, showing (a) the real values, (b) the imaginary values, and (c) the absolute values.

$\theta = 0°$

(a)

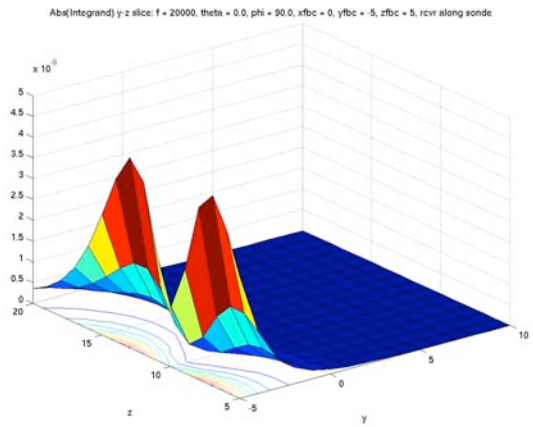

$\theta = 45°$

(b)

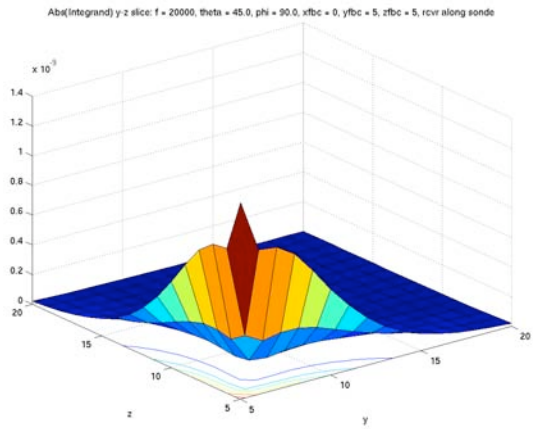

$\theta = 90°$

(c)

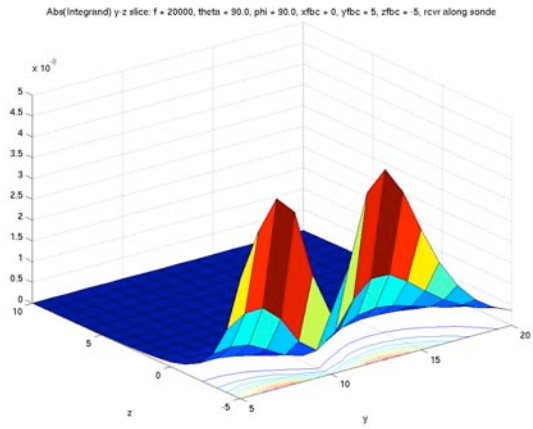

Figure 30: The integrand in the frequency domain for tool 1, transmitter dipole and receiver dipole in the direction of the tool orientation. Frequency = 20,000 Hz, wholespace conductivity = 0.25 S/m, in the *y*-*z* plane 5 meters away from the fault boundary corner for (a) the vertical sonde, (b) the sonde dipping at 45˚, and (c) the horizontal sonde.

(a)

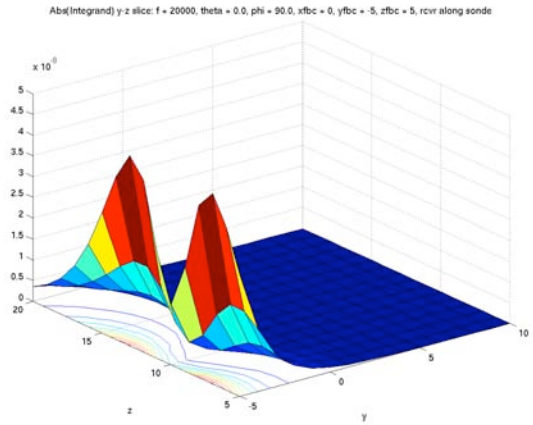

(b)

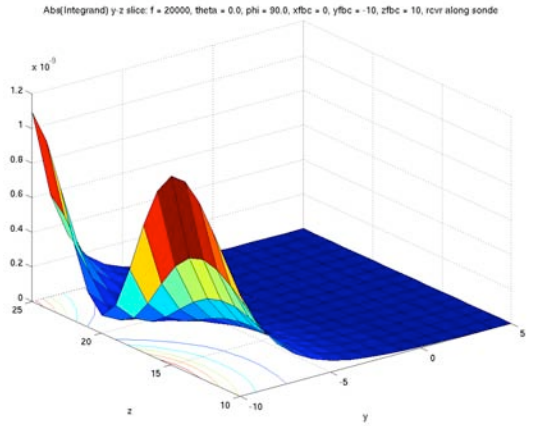

Figure 31: The integrand in the frequency domain for tool 1, transmitter dipole and receiver dipole in the direction of the tool orientation. Frequency = 20,000 Hz, wholespace conductivity = 0.25 S/m, for the vertical sonde in the *y-z* plane (a) 5 meters, and (b) 10 meters away from the fault boundary corner.

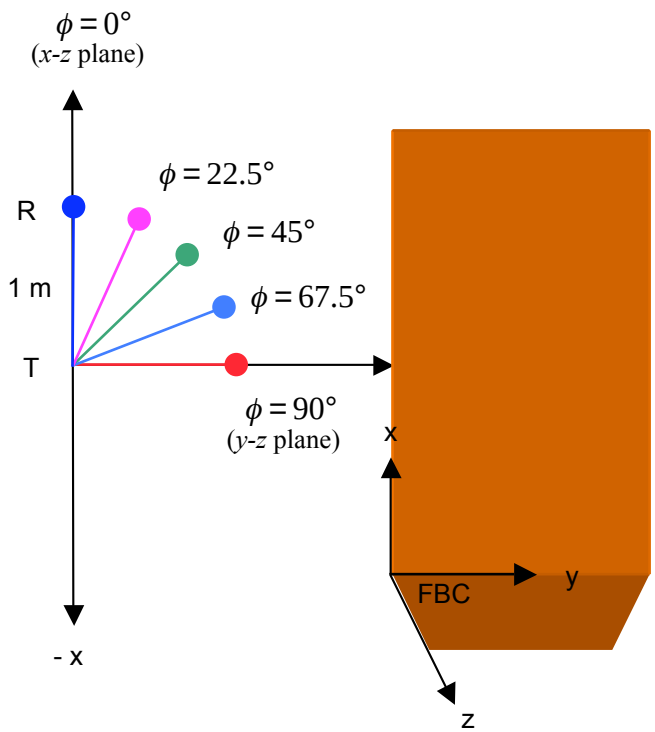

Figure 32: Map projection of the fault boundary corner. Sensitivities in the frequency domain for tool 2, transmitter dipole in the tool orientation and receiver dipole with the *x,y,z* coordinates relative to the sonde direction. Sensitivities in the oblique planes around the fault boundary corner were calculated from zero to 20 meters, in one-meter intervals in the *x-z* plane (ϕ = 0˚), angled at 22.5˚ (ϕ= 22.5˚), 45˚ (ϕ= 45˚), 67.5˚ (ϕ= 67.5˚), and in the *y-z* plane, (ϕ = 90˚).

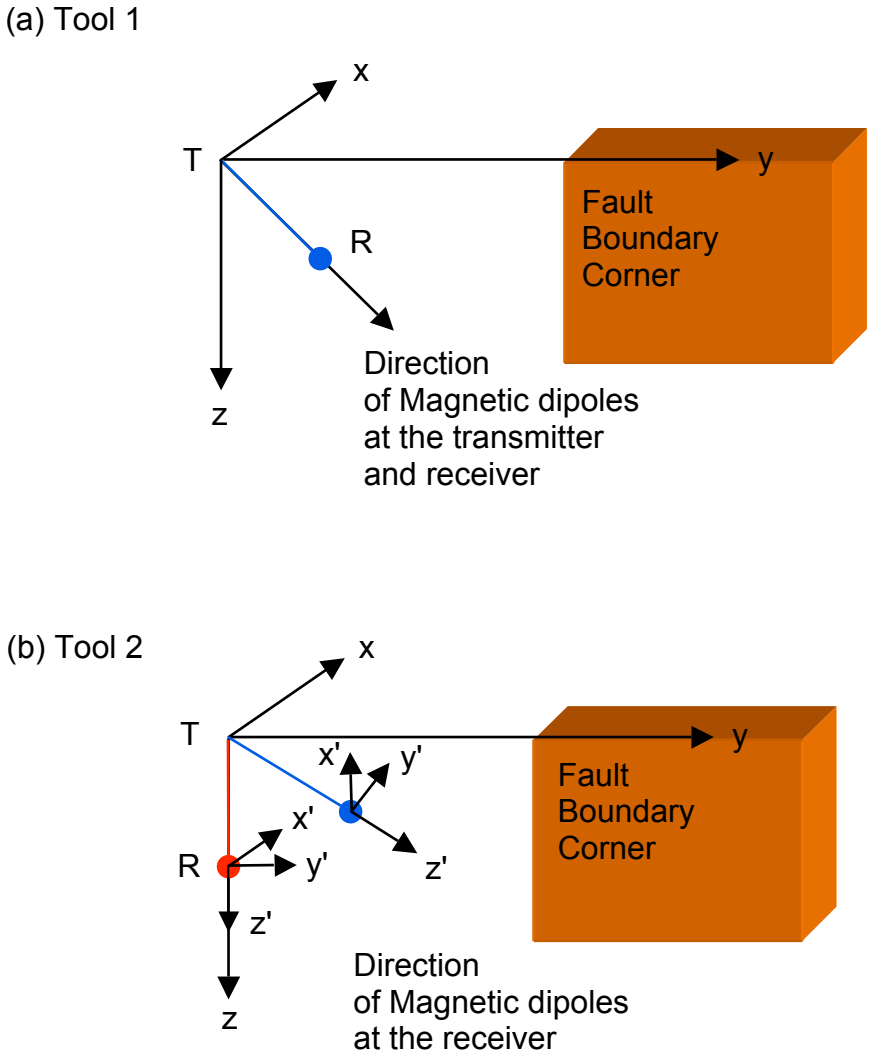

Figure 33: Tool locations around the fault boundary corner. Sensitivities in the frequency domain were calculated for (a) tool 1, transmitter and receiver dipoles in the direction of the tool orientation and (b) tool 2, transmitter dipole in the direction of the receiver and an *x,y, or z*-directed magnetic dipole at the receiver. In this case the orientation of the dipole at the receiver (x,y,z directions) are relative to the sonde axis.

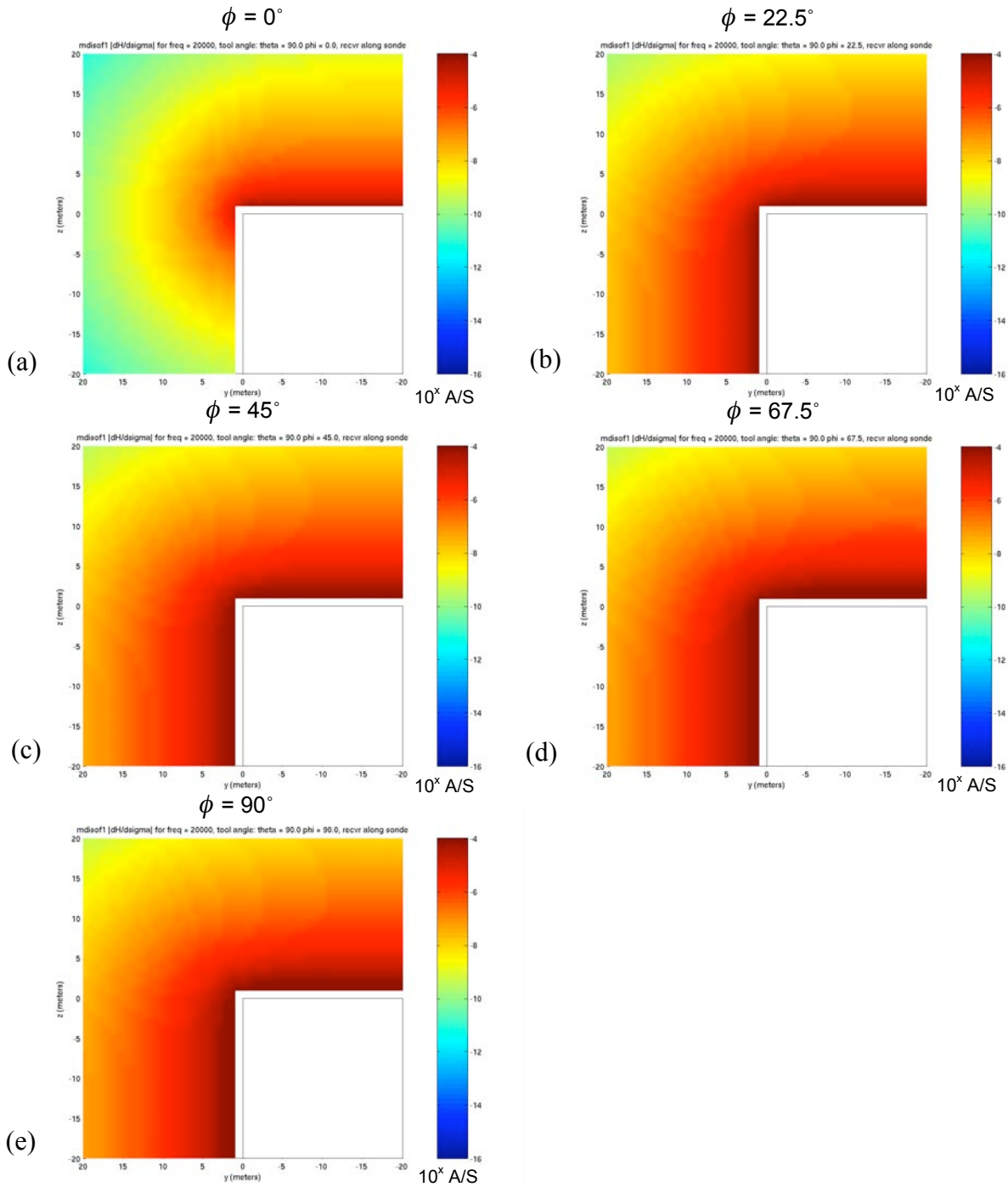

Figure 34: Sensitivities in the frequency domain for tool 1, transmitter dipole and receiver dipole in the direction of the sonde. Sensitivities in the oblique planes around the fault boundary corner were calculated from zero to 20 meters, in one-meter intervals. Frequency = 20,000 Hz, wholespace conductivity = 0.25 S/m, for the horizontal sonde in the (a) *x-z* plane, (b) angled at 22.5° (ϕ= 22.5°), (c) 45° (ϕ= 45°), (d) 67.5 ° (ϕ= 67.5°), and (e) 90° (ϕ = 90°).

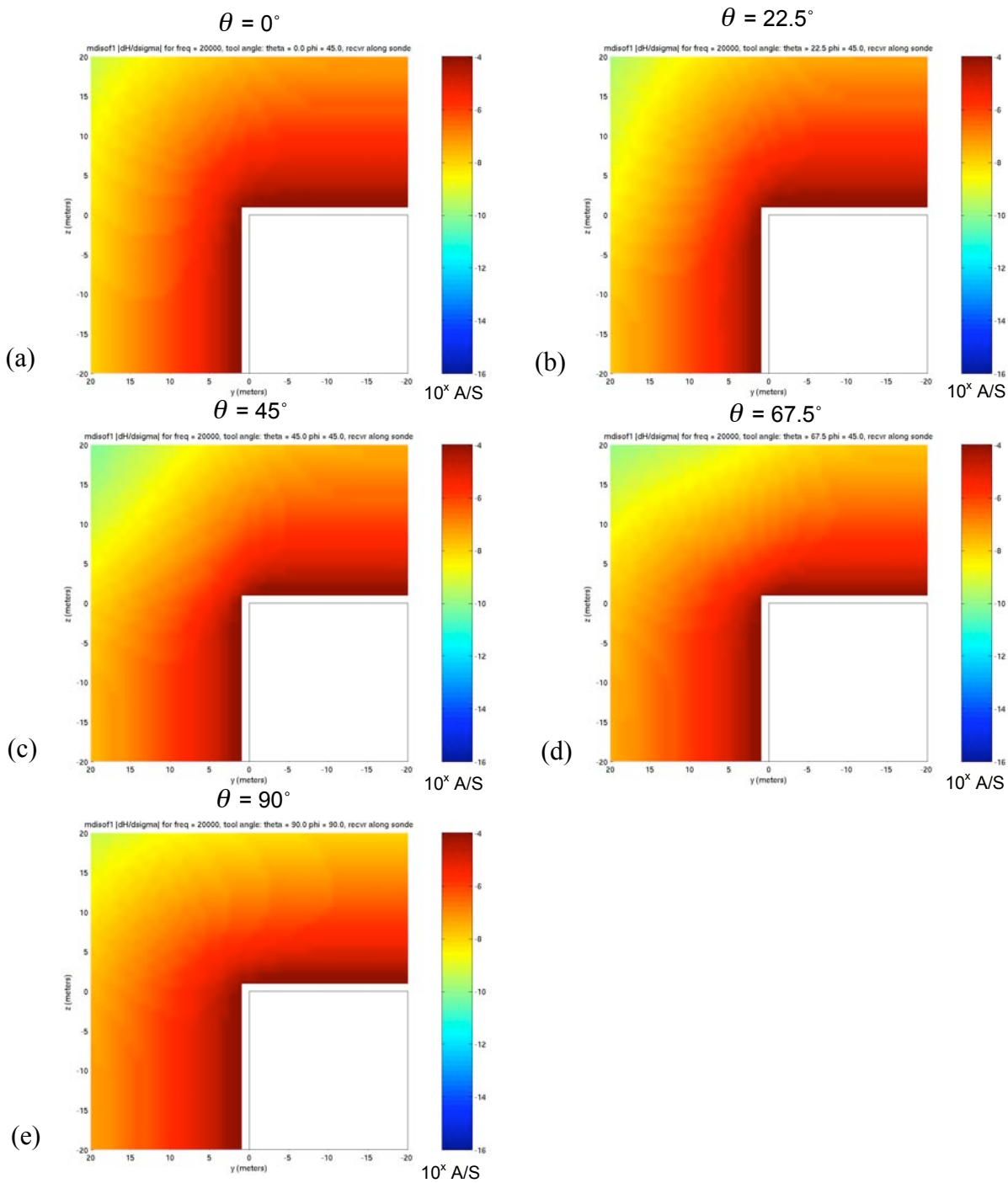

Figure 35: Sensitivities in the frequency domain for tool 1, transmitter dipole and receiver dipole in the direction of the sonde. Sensitivities were calculated in the plane angled at $\phi = 45^\circ$. Frequency = 20,000 Hz, wholespace conductivity = 0.25 S/m, for (a) the vertical sonde ($\theta = 0^\circ$), (b) the sonde dipping at 22.5°($\theta = 22.5^\circ$), (c) 45°($\theta = 45^\circ$), (d) 67.5°($\theta = 67.5^\circ$), and (e) the horizontal sonde ($\theta = 90^\circ$).

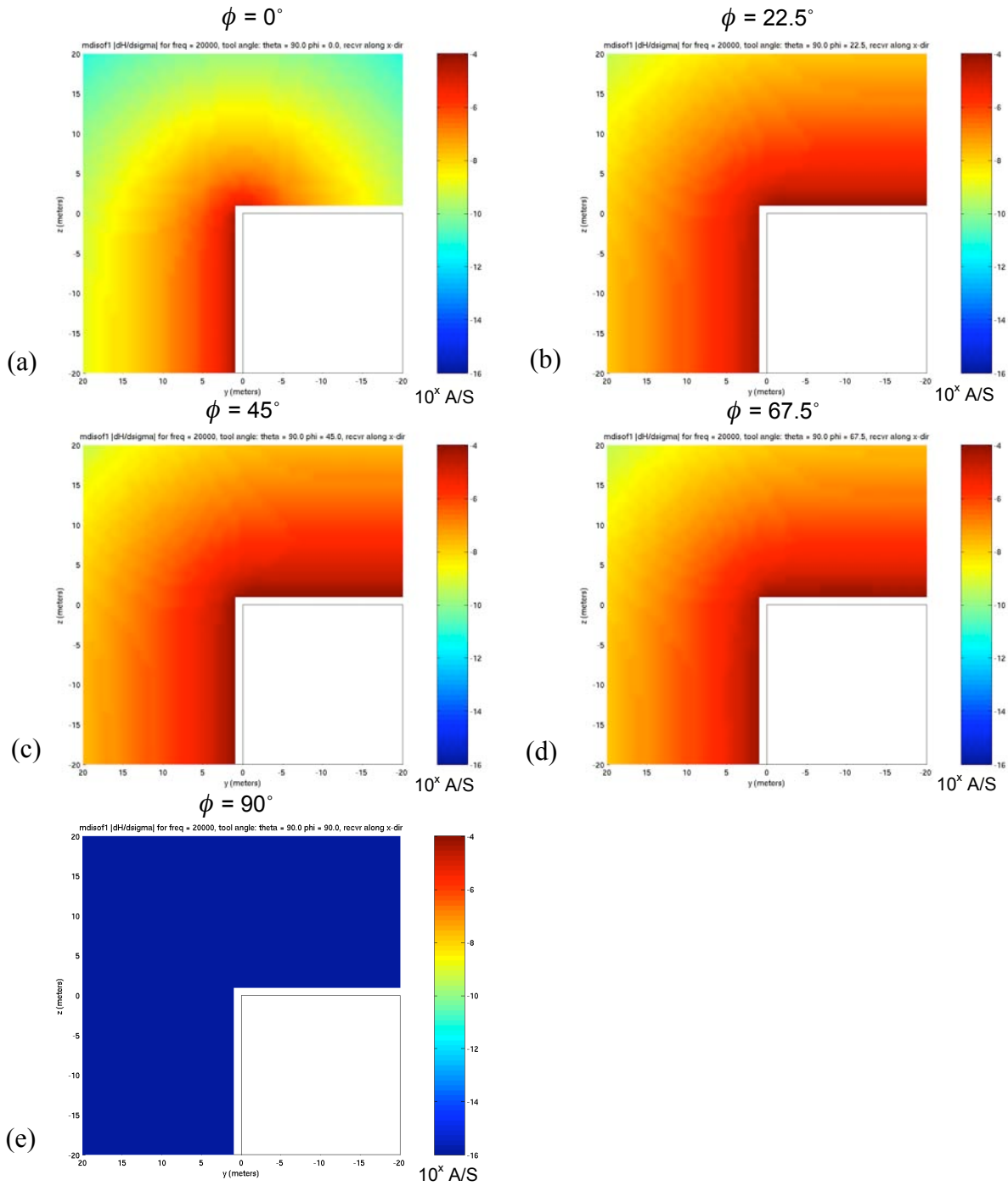

Figure 36: Sensitivities in the frequency domain for tool 2, transmitter dipole in the tool orientation and receiver dipole in the *x*-direction with the *x,y,z* coordinates relative to the sonde direction. Sensitivities in the oblique planes around the fault boundary corner were calculated from zero to 20 meters, in one-meter intervals. Frequency = 20,000 Hz, wholespace conductivity = 0.25 S/m, for the horizontal sonde in the (a) *x*-*z* plane, (b) angled at 22.5° (ϕ= 22.5°), (c) 45° (ϕ= 45°), (d) 67.5 ° (ϕ= 67.5°), and (e) 90° (ϕ = 90°).

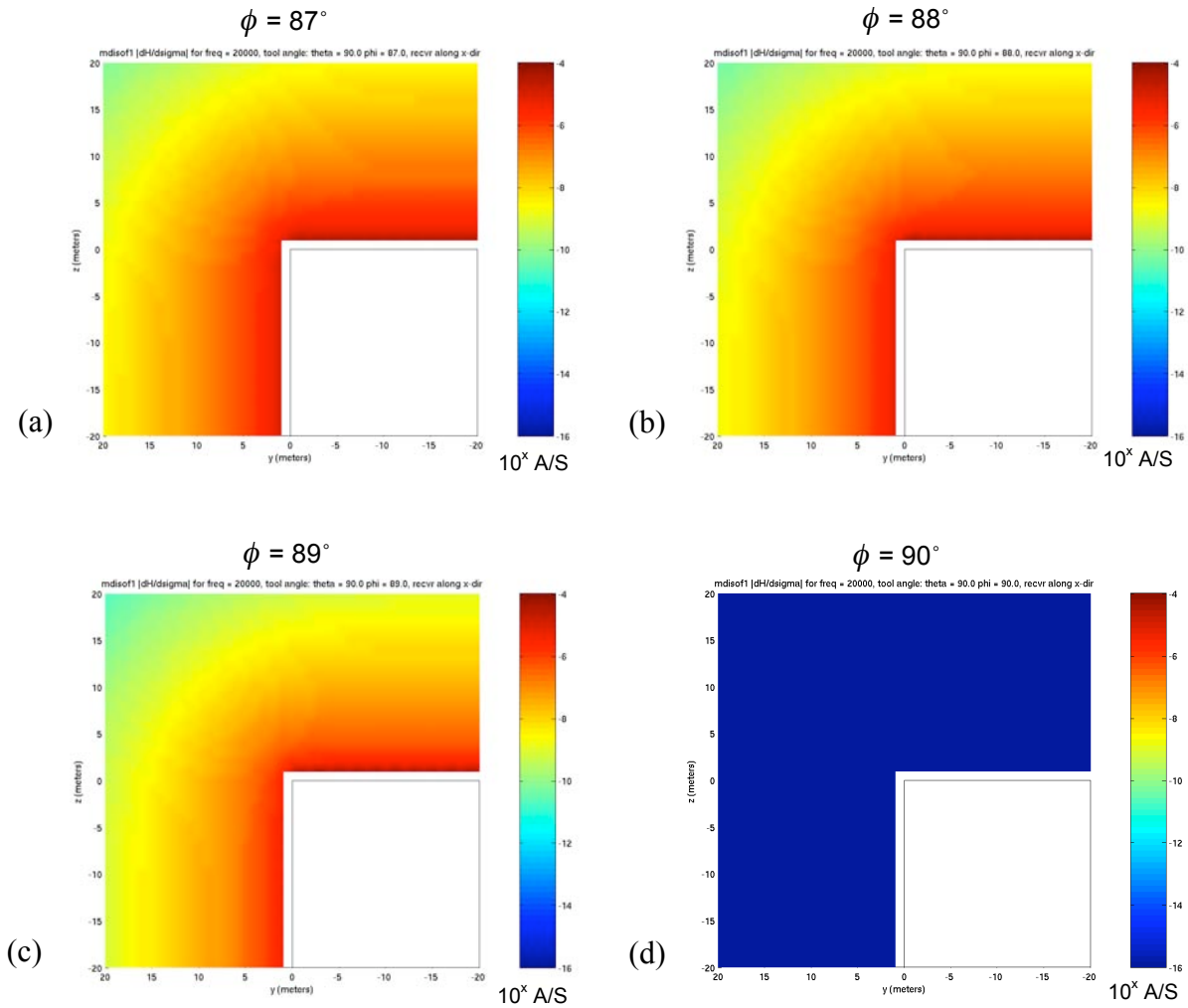

Figure 37: Sensitivities in the frequency domain for tool 2, transmitter dipole in the tool orientation and receiver dipole in the *x*-direction with the *x,y,z* coordinates relative to the sonde direction. Sensitivities in the oblique planes around the fault boundary corner were calculated from zero to 20 meters, in one-meter intervals. Frequency = 20,000 Hz, wholespace conductivity = 0.25 S/m, for the horizontal sonde, angled at (a) 87° (ϕ = 87°), (b) 88° (ϕ = 88°), (c) 89° (ϕ = 89°) from the *x*-*z* plane, and (d) in the *y*-*z* plane, 90° (ϕ = 90°).

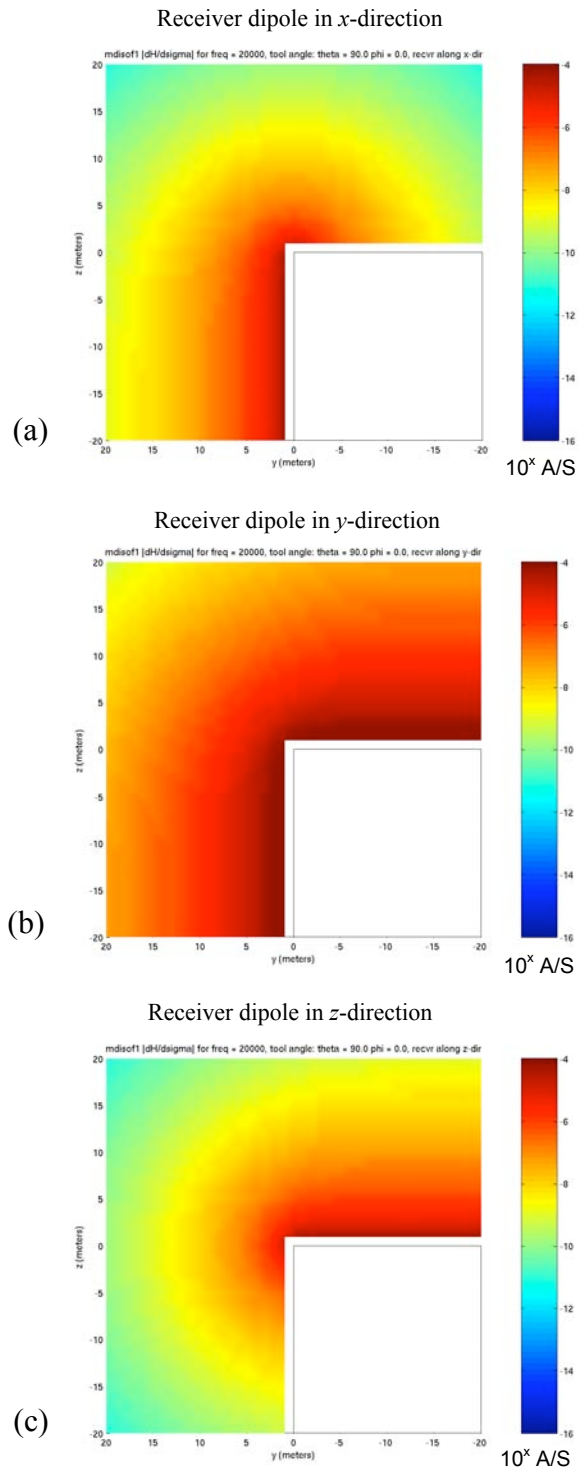

Figure 38: Sensitivities in the frequency domain for tool 2, transmitter dipole in the tool orientation and receiver dipole with the *x,y,z* coordinates relative to the sonde direction. Sensitivities in the oblique planes around the fault boundary corner were calculated from zero to 20 meters, in one-meter intervals. Frequency = 20,000 Hz, wholespace conductivity = 0.25 S/m, for the horizontal sonde parallel to the FBC with the receiver dipole in the (a) *x*-direction, (b) *y*-direction, and (c) in the *z*-direction.

$$\frac{\partial^2 \pi_y}{\partial x^2} + \frac{\partial^2 \pi_y}{\partial y^2} + \frac{1}{\lambda^2}\frac{\partial^2 \pi_y}{\partial z^2} + i\omega\mu_o\sigma_v\pi_y = -\frac{M_y}{\lambda^2}, \tag{B14}$$

and

$$\frac{\partial^2 \pi_z}{\partial x^2} + \frac{\partial^2 \pi_z}{\partial y^2} + \frac{1}{\lambda^2}\frac{\partial^2 \pi_z}{\partial z^2} + i\omega\mu_o\sigma_h\pi_z = -M_z + \left(1-\lambda^2\right)\frac{\partial}{\partial z}\left(\frac{\partial \pi_x}{\partial x} + \frac{\partial \pi_y}{\partial y}\right),$$

where M_x, M_y, M_z are the components of the dipole source $\vec{M}_s$.

The solution to the above set of coupled PDEs can be obtained in terms of simple analytic functions (Moran and Gianzero, 1979) that we present below in Table 1, for the three separate cases of the magnetic dipole pointing along the coordinate axes. Since Maxwell's equations are linear, the solutions for the Hertz potentials for an arbitrarily oriented magnetic dipole can be built up from superposition. Once the scalar potential Φ and the Hertz potential $\vec{\pi}$ are obtained from Table 1, the resulting electric and magnetic fields are obtained from Eq.(B12) and Eq.(B13) by straightforward differentiation.

Table 1. Hertz vector for a magnetic dipole in a homogeneous anisotropic case.

$\lambda^2 = \frac{\sigma^h}{\sigma^v}$ $\qquad$ $r = \sqrt{x^2 + y^2 + x^2}$

$k_h^2 = i\omega\mu\sigma_h$ $\qquad$ $s = \sqrt{x^2 + y^2 + \lambda^2 z^2}$

$k_v^2 = i\omega\mu\sigma_v$ $\qquad$ $p = \sqrt{x^2 + y^2}$

For an *x*-directed dipole – source along *x*:

$M_x = M,\ M_y = M_z = 0$

$$\pi_x = \frac{M}{4\pi\lambda}\frac{e^{ik_v s}}{s}$$

$$\pi_y = 0$$

$$\pi_z = \frac{M}{4\pi}\frac{x}{\rho^2}\left(\lambda z\frac{e^{ik_v s}}{s} - z\frac{e^{ik_h r}}{r}\right)$$

$$\Phi = \frac{M}{4\pi}\frac{ik_h x}{\rho^2}\left(e^{ik_v s} - e^{ik_h r}\right) + \frac{\rho^2}{r^2}\left(1 - \frac{1}{ik_h r}\right)e^{ik_h r}$$

For an y-directed dipole – source along y:

$$M_y = M,\ \ M_x = M_z = 0$$

$$\pi_x = 0$$

$$\pi_y = \frac{M}{4\pi\lambda}\frac{e^{ik_v s}}{s}$$

$$\pi_z = \frac{M}{4\pi}\frac{y}{\rho^2}\left(\lambda z\frac{e^{ik_v s}}{s} - z\frac{e^{ik_h r}}{r}\right)$$

$$\Phi = \frac{M}{4\pi}\frac{ik_h y}{\rho^2}\left(e^{ik_v s} - e^{ik_h r}\right) + \frac{\rho^2}{r^2}\left(1 - \frac{1}{ik_h r}\right)e^{ik_h r}$$

For an z-directed dipole – source along z:

$$M_z = M,\ \ M_x = M_y = 0$$

$$\pi_x = 0$$

$$\pi_y = 0$$

$$\pi_z = \frac{M}{4\pi}\frac{e^{ik_h r}}{r}$$

$$\Phi = \frac{M}{4\pi}\frac{ik_h z}{r^2}\left(1 - \frac{1}{ik_h r}\right)e^{ik_h r}$$

APPENDIX B

The Numerical Code

The following numerical codes are attached in hard copy and electronic form for the Sandia National Laboratories copy of this report only. Details concerning code methodology, code execution and input files are contained in the driver code README_mdisof1 file.

Fortran 95 codes:

mdisof1.f	Driver code for the magnetic dipole isotropic quarterspace model in the frequency domain
globals_mdisof1.f	Globals module
integration_routines.f	Fourth order Simpson integration module
mdisof1.in	Input file
README_mdisof1	Read me file

Fortran 77 codes (Weiss, 2002) modified by Natek:

mdisof1_efield_routines.f	Module to calculate the electric fields for the anisotropic wholespace model
mdisof1_mfield_routines.f	Module to calculate the magnetic fields for the anisotropic wholespace model

Matlab codes:

make_mdisof1_filename.m	Matlab function to make mdisof1 input filenames
make_mdisof1_run_jobs.m	Creates multiple mdisof1_xx_xx_xx.in files for the mdisof1 code
plot_mdisof1_colorpatch_dHdsigma_ReIm.m	Creates colorpatch plots of the absolute values of the sensitivities from the mdisof1 output file mdisof1_all.out.